Structures 58 (2023) 105408

Contents lists available at ScienceDirect

Structures

journal homepage: www.elsevier.com/locate/structures

# Simplified optimization of inerter-enabled tuned mass damper for lightweight-oriented seismic response mitigation of long-span domes

Jianfei Kang [a], Liyu Xie [a,*], Songtao Xue [a,b], Zhipeng Zhao [a]

[a] Department of Disaster Mitigation for Structures, Tongji University, Shanghai 200092, China
[b] Department of Architecture, Tohoku Institute of Technology, Sendai 982-8577, Japan

ARTICLE INFO

*Keywords:*
Inerter
Tuned mass damper
Lightweight control
Long-span dome

ABSTRACT

Suspending tuned mass dampers (TMDs) from long-span domes has been studied to mitigate seismic responses of long-span domes. However, the strict weight limitations on the suspension mass in conventional tuned mass dampers (TMDs) hinder their widespread adoption. To address this issue, we introduce the inerter-enabled tuned mass damper (IeTMD) that consists of a suspension mass, tuning spring, and a tuned viscous mass damper (TVMD) sub-system into the seismic vibration mitigation of long-span domes. Under the assumption that long-span domes remain within the elastic range and adhere to the small deformation hypothesis, we have proposed simplified design formulae for IeTMDs, guided by the lightweight-based seismic vibration control criterion. Parametric studies are conducted to illustrate the degree to which an IeTMD can improve the performance of the long-span dome when its key parameters change within certain ranges. The effectiveness of the design strategy in exploiting the damping enhancement effect is confirmed. Time history responses of a benchmark long-span dome demonstrate that the IeTMD has high control efficiency, as bi-directional displacements, accelerations, and base shear are significantly reduced. Comparative analyses between the proposed IeTMD and conventional TMD are conducted. Results show that the IeTMD designed by the simplified design formulae can achieve the target control performance with less suspension mass. Furthermore, the frequency analysis shows that the proposed IeTMD contains a wider control frequency band than conventional TMD, illustrating the promising approach for long-span domes.

## 1. Introduction

Long-span structures covering vast spaces have fascinated generations of engineers. Until recent centuries, the completion of comprehensive knowledge in mechanics and development of construction technology enabled long-span domes to be applied to various public buildings for the synthetic function of commercial and recreational ones [1]. With the appropriate form-finding design, the capacity of long-span domes for bearing vertical gravity can be obtained. However, limited by its little inherent damping, the long-span domes may experience significant vibrations and deformations subjected to dynamic loads, such as earthquakes [2–7]. Lessons from the reported damages of long-span domes during the Kobe Earthquake of 1995 [8], the Wenchuan Earthquake of 2008 [9], and the Tohoku Earthquake of 2011 [10] urge engineers to pay attention to the seismic response mitigation of long-span domes. Public buildings with long-span domes are usually the first choice for temporary shelter after an earthquake [11], further increasing the need to guarantee their seismic performance.

Ishikawa and Kato [4] examined the dynamic properties of single-layer reticular domes and proposed an empirical function of the safety factor against gravity loading for estimating collapse accelerations. Kato et al. [5] noted that, in contrast to conventional building structures, significant anti-symmetric vertical responses play a crucial role in the vibration of long-span domes even when subjected to horizontal ground motions. Takeuchi et al. [12,13] proposed amplification factors to estimate the seismic responses of long-span domes, considering their interaction with the supporting structures. Thus, through numerical analysis and shaking table experiments, the failure mechanisms of various types of long-span structures subjected to severe earthquakes [14–19] have been understood. An increasing number of response control techniques [20–23] have been implemented to improve the performance of long-span domes subjected to ground disturbances. The tuned mass damper (TMD) has been extensively studied due to its straightforward fabrication and installation procedures. Tsuda and

* Corresponding author.
*E-mail address:* liyuxie@tongji.edu.cn (L. Xie).

https://doi.org/10.1016/j.istruc.2023.105408
Received 1 June 2023; Received in revised form 24 September 2023; Accepted 16 October 2023
Available online 21 October 2023

Ohsaki [24] invented a three-degree-of-freedom TMD by combining three springs, a viscous damper, and a suspension mass to control the vibration of long-span structures under the excitation of bi-directional ground motions. Yoshinaka and Kawaguchi [25] proposed spatially dispersed multiple TMDs for controlling multiple modes of long-span domes within a particular frequency band. Therefore, by solving a mixed integer programming (MIP) problem, Yamakawa et al. [26] obtained the spatial arrangement and optimal parameters of multiple TMDs simultaneously. Nonetheless, the upper limit of the suspension mass ratio, the ratio between the suspension mass and the primary domes' mass, e.g., 1–5 % [24], still impedes the application of TMD for seismic response control of long-span domes, especially in the retrofitting scenario. In addition, the robustness of TMD must be further improved to address the challenge posed by the closely spaced modes inherent to long-span domes.

Recently, inerter, a mechanical element that generates a resistant force proportional to the relative acceleration between its two independent terminals [27–34], has garnered the attention of researchers as a possible solution to the problems mentioned above associated with conventional TMDs. Kawamata's liquid mass pump [35], proposed in the 1970s, is the precursor to the two-terminal acceleration-based device in civil engineering. In 1999, Arakaki et al. [36,37] introduced a series of rotary dampers that utilized ball screws to convert the linear movements of the damper into the high-speed rotational motion of its inner tube. Later, Saito et al. [38] developed the tuned viscous mass damper (TVMD) by adding a flywheel to the rotary damper to intentionally take advantage of the apparent mass amplification effect caused by the inner tube's rotation. Ikago et al. [39] extended the fixed-point method, commonly used for conventional TMDs, to the TVMD. Through theoretical and experimental analysis, they demonstrated that the TVMD outperforms the VMD and viscous damper. As reported, the TVMD has already been implemented in high-rise buildings in Sendai [40] and Tokyo [41]. Besides, Lazar et al. [42] investigated a different type of inerter-based device called a tuned inerter damper (TID), which shares the same configuration as conventional TMDs. Zhang et al. [43] clarified the correlation between the damping enhancement effect and the response mitigation effect of inerter-based devices. Djerouni et al. [44] connected two rooftop TMDs with an inerter, proposing the concept of a double mass tuned damper inerter, which was validated using one hundred near and far-field ground motions to assess its seismic mitigation performance. Furthermore, Djerouni et al. [45] have also proven the effectiveness of inerter-based devices in mitigating pounding of adjacent buildings.

Additionally, Giaralis and Marian [46] and De Domenico and Ricciardi [47] improved the performance of the TMD by integrating it with the primary structure through an inerter, resulting in a tuned mass damper inerter (TMDI). However, the grounded connection form hinders the broad applications of TMDI, especially the long-span domes. Garrido et al. [48] suggested employing a TVMD-like sub-system as the energy dissipation element in a TMD, known as the rotational inertia double-tuned mass damper (RIDTMD). They demonstrated the superior control effectiveness of RIDTMD on a single-degree-of-freedom system compared to a conventional TMD. Barredo et al. [49–51] extended Den Hartog's technique to derive closed-form design formulae for three distinct types of inerter-enabled TMDs (IeTMDs). Zhang et al. [52,53] investigated the lightweight control effect of IeTMD for wind turbine towers under the influence of ground motions and wind loads. Zhang and Larsen [54] derived optimal calibration formulae for the RIDTMD, based on the pole-placement method, for controlling the rotation of wind turbine blades. Despite the lightweight potential of IeTMD, there is still uncertainty surrounding its implementation in long-span domes. A practical design method for the long-span domes equipped with IeTMDs is also desirable.

In this study, we introduce a well-developed and small-scale IeTMD to mitigate the seismic response of long-span domes. Under the assumption that long-span domes remain within the elastic range and adhere to the small deformation hypothesis, easy-to-use and simplified design formulae are proposed for IeTMD to facilitate the lightweight-control-oriented design criterion and desired control performances. Then, we conducted parametric and comparative studies to illustrate the effectiveness and efficiency of the proposed design method.

## 2. Basic concepts of long-span dome equipped with IeTMDs

With the rapid development of long-span domes for the synthetic functions of commercial and recreational ones, high-performance long-span domes are preferable in constructing resilient cities. This section introduces the well-developed and small-scale IeTMD, including its suspending method, mechanical model, and physical realization. Then, the mechanical model of the original and IeTMD-equipped long-span domes is established, together with its governing equation for the finite element analysis in this study.

### 2.1. IeTMD model

The prototype example in Fig. 1(a) demonstrates how the suspending IeTMD is quite compactly realizable. Two springs with different stiffnesses connecting the dome's suspension point to the external tube and the ball screw, respectively, can tune the suspension mass and the inherent TVMD-like substructure to specific frequencies. The ball screw and nut convert the tuning spring's linear motion into the internal tube's rotation to achieve amplified inertia, realizing the inerter mechanism. Meanwhile, the viscous material filling the external and internal tube gaps is utilized as an energy dissipation element. The idealized mechanical model of the IeTMD is shown in Fig. 1(b), where $k_t$ and $k_{in}$ represent two springs' stiffnesses, respectively. The thickness and type of the viscous material affect the damping coefficient ($c_{in}$), a measure of the energy dissipation element. $m_{in}$ is the apparent mass of the inerter element, determined by the ball screw's lead length [39]. $m_t$ is the suspension mass of the IeTMD, which equals the device's total physical mass.

Assuming the vertical displacement of the suspension mass and that of the ball screw are $u_t$ and $u_{in}$, respectively, the governing motion equations of the IeTMD can be expressed as:

$$\begin{cases} m_t\ddot{u}_t = k_t(u_t - u_0) + k_{in}(u_{in} - u_0) \\ k_{in}(u_{in} - u_0) = c_{in}\left(\dot{u}_t - \dot{u}_{in}\right) + m_{in}\left(\ddot{u}_t - \ddot{u}_{in}\right) \end{cases} \tag{1}$$

where $u_0$ is the vertical displacement of the dome's suspension point.

Note that when linking the ball screw directly to the dome's suspension point ($k_{in} = \infty$) and minimizing the apparent mass $m_{in}$ ($m_{in} = 0$), the IeTMD will be converted to a conventional TMD, and the governing motion equations are:

$$m_t\ddot{u}_t = k_t(u_t - u_0) + c_{in}\left(\dot{u}_t - \dot{u}_0\right) \tag{2}$$

### 2.2. Long-span dome model

Fig. 2 depicts the models of the long-span domes with and without a suspension IeTMD in OpenSees. $H$, $h$, and $L$ denote the column height, the dome's rise, and the dome's span, respectively. $R$ and $\theta$ symbolize the dome's radius and half-subtended angle, respectively. An assemblage of elastic beam elements with concentrated translational node masses is adopted to accelerate the computational efficiency needed to simulate the long-span domes. $E$, $A$, and $I$ are Young's modulus of the material, cross-sectional area, and section's second moment of the arch beams and column legs. The motion equations of the primary dome subjected to ground motion can be expressed as follows:

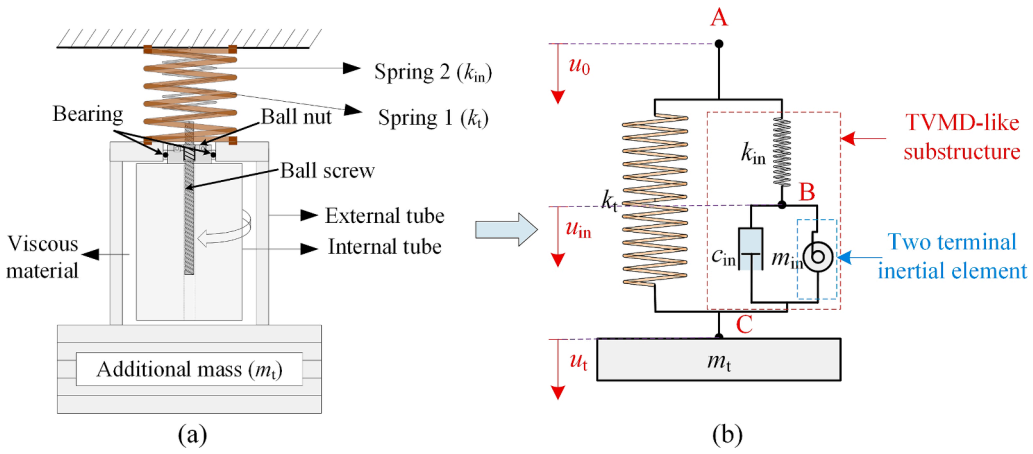


**Fig. 1.** IeTMD: (a) prototype example (b) mechanical model.

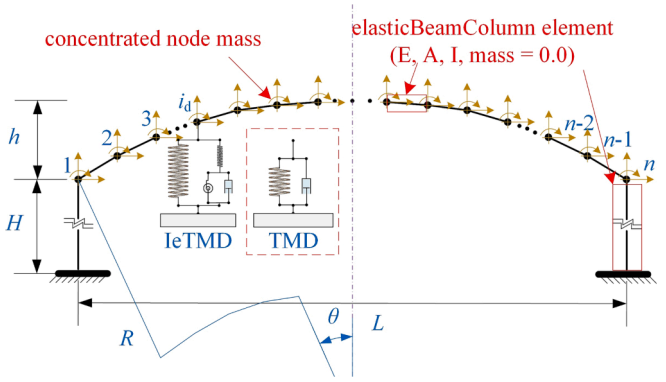


**Fig. 2.** Long-span domes with and without a suspension IeTMD (in OpenSees).

$$[\boldsymbol{M}_{\mathrm{p}}]_{3n\times 3n}\begin{Bmatrix}\ddot{x}_{\mathrm{p}}\\ \ddot{y}_{\mathrm{p}}\\ \ddot{\theta}_{\mathrm{p}}\end{Bmatrix}+[\boldsymbol{C}_{\mathrm{p}}]_{3n\times 3n}\begin{Bmatrix}\dot{x}_{\mathrm{p}}\\ \dot{y}_{\mathrm{p}}\\ \dot{\theta}_{\mathrm{p}}\end{Bmatrix}+[\boldsymbol{K}_{\mathrm{p}}]_{3n\times 3n}\begin{Bmatrix}x_{\mathrm{p}}\\ y_{\mathrm{p}}\\ \theta_{\mathrm{p}}\end{Bmatrix}=[\boldsymbol{M}_{\mathrm{p}}]_{3n\times 3n}\{\boldsymbol{r}\}_{3n\times 1}\ddot{x}_g \tag{3}$$

where, $n$ is the number of the dome's discrete nodes. The horizontal, vertical, and rotational displacements of the dome's discrete nodes are denoted by $x_{\mathrm{p}}$, $y_{\mathrm{p}}$, and $\theta_{\mathrm{p}}$, respectively. $[\boldsymbol{M}_{\mathrm{p}}]_{3n\times 3n}$, $[\boldsymbol{K}_{\mathrm{p}}]_{3n\times 3n}$, and $[\boldsymbol{C}_{\mathrm{p}}]_{3n\times 3n}$ are the dome's mass, stiffness, and damping matrices, respectively:

$$[M_p]_{3n\times 3n}=\begin{bmatrix}M_{p,x} & & \\ & M_{p,y} & \\ & & M_{p,\theta}\end{bmatrix} \tag{4}$$

$$[K_p]_{3n\times 3n}=\begin{bmatrix}K_{p,x,x} & K_{p,x,y} & K_{p,x,\theta}\\ K_{p,y,x} & K_{p,y,y} & K_{p,y,\theta}\\ K_{p,\theta,x} & K_{p,\theta,y} & K_{p,\theta,\theta}\end{bmatrix} \tag{5}$$

$$\left[\boldsymbol{C}_{\mathrm{p}}^{\mathrm{c}}\right]_{2n\times 2n}=\alpha_1\left[\boldsymbol{M}_{\mathrm{p}}^{\mathrm{c}}\right]_{2n\times 2n}+\alpha_2\left[\boldsymbol{K}_{\mathrm{p}}^{\mathrm{c}}\right]_{2n\times 2n} \tag{6}$$

where, $\boldsymbol{M}_{\mathrm{p,x}}$, $\boldsymbol{M}_{\mathrm{p,y}}$, and $M_{p,\theta}$ are diagonal matrices denoting the horizontal, vertical, and rotational masses of the dome's discrete nodes [24]. $\alpha_1$ and $\alpha_2$ are the Rayleigh coefficients.

Ignoring the rotational masses of the dome's discrete nodes [55], which contribute less to the seismic responses, Eq. (3) can be further simplified with static condensation:

$$\left[\boldsymbol{M}_{\mathrm{p}}^{\mathrm{c}}\right]_{2n\times 2n}\begin{Bmatrix}\ddot{x}_{\mathrm{p}}\\ \ddot{y}_{\mathrm{p}}\end{Bmatrix}+\left[\boldsymbol{C}_{\mathrm{p}}^{\mathrm{c}}\right]_{2n\times 2n}\begin{Bmatrix}\dot{x}_{\mathrm{p}}\\ \dot{y}_{\mathrm{p}}\end{Bmatrix}+\left[\boldsymbol{K}_{\mathrm{p}}^{\mathrm{c}}\right]_{2n\times 2n}\begin{Bmatrix}x_{\mathrm{p}}\\ y_{\mathrm{p}}\end{Bmatrix}=\left[\boldsymbol{M}_{\mathrm{p}}^{\mathrm{c}}\right]_{2n\times 2n}\{\hat{\boldsymbol{r}}\}_{2n\times 1}\ddot{x}_g \tag{7}$$

where,

$$\left[\boldsymbol{M}_{\mathrm{p}}^{\mathrm{c}}\right]_{2n\times 2n}=\begin{bmatrix}\boldsymbol{M}_{\mathrm{p,x}} & \\ & \boldsymbol{M}_{\mathrm{p,y}}\end{bmatrix} \tag{8}$$

$$\left[K_p^c\right]_{2n\times 2n}=\begin{bmatrix}K_{p,x,x} & K_{p,x,y}\\ K_{p,y,x} & K_{p,y,y}\end{bmatrix}-\begin{bmatrix}K_{p,x,\theta}\\ K_{p,y,\theta}\end{bmatrix}K_{p,\theta,\theta}^{-1}\begin{bmatrix}K_{p,\theta,x} & K_{p,\theta,y}\end{bmatrix} \tag{9}$$

$$\left[\boldsymbol{C}_{\mathrm{p}}^{\mathrm{c}}\right]_{2n\times 2n}=\alpha_1\left[\boldsymbol{M}_{\mathrm{p}}^{\mathrm{c}}\right]_{2n\times 2n}+\alpha_2\left[\boldsymbol{K}_{\mathrm{p}}^{\mathrm{c}}\right]_{2n\times 2n} \tag{10}$$

For long-span domes, $\mathbf{K}_{\mathrm{p,x,y}}$, $\mathbf{K}_{\mathrm{p,x,x}}$, and $\mathbf{K}_{\mathrm{p,y,y}}$ in Eqs. (5) and (9) are of nearly the same order of magnitude. Long-span domes, in contrast to conventional building structures, display a heightened coupling between horizontal and vertical vibrations [5]. This implies that effective control of the dome's horizontal and vertical vibrations can be achieved by installing IeTMDs in either a horizontal or vertical orientation. To simplify installation, IeTMDs are vertically suspended directly from the long-span dome, as illustrated in Fig. 2.

By combining the motion equations of the primary dome subject to ground motion (Eq. (3)) with the IeTMD motion equations (Eq. (1)), we can obtain the motion equations of the dome under the control of the IeTMDs:

$$[\boldsymbol{M}]\begin{Bmatrix}\ddot{x}_{\mathrm{p}}\\ \ddot{y}_{\mathrm{p}}\\ \ddot{y}_{\mathrm{in}}\\ \ddot{y}_{\mathrm{t}}\end{Bmatrix}+[\boldsymbol{C}]\begin{Bmatrix}\dot{x}_{\mathrm{p}}\\ \dot{y}_{\mathrm{p}}\\ \dot{y}_{\mathrm{in}}\\ \dot{y}_{\mathrm{t}}\end{Bmatrix}+[\boldsymbol{K}]\begin{Bmatrix}x_{\mathrm{p}}\\ y_{\mathrm{p}}\\ y_{\mathrm{in}}\\ y_{\mathrm{t}}\end{Bmatrix}=[\boldsymbol{M}_0]\{\hat{\boldsymbol{r}}\}\ddot{x}_g \tag{11}$$

$$[\boldsymbol{M}]=\begin{bmatrix}\boldsymbol{M}_{\mathrm{p,x}}+\boldsymbol{R}_{\mathrm{c}}\boldsymbol{M}_{\mathrm{t}}\boldsymbol{R}_{\mathrm{c}}^{T} & & \\ & \boldsymbol{M}_{\mathrm{p,y}} & \\ & & \begin{matrix}\boldsymbol{M}_{\mathrm{t}}+\boldsymbol{M}_{\mathrm{in}} & -\boldsymbol{M}_{\mathrm{in}}\\ -\boldsymbol{M}_{\mathrm{in}} & \boldsymbol{M}_{\mathrm{in}}\end{matrix}\end{bmatrix} \tag{12}$$

$$[\boldsymbol{K}]=\begin{bmatrix} \boldsymbol{K}_{\mathrm{p}}^{\mathrm{c}}+\begin{bmatrix}\boldsymbol{0}_{\mathrm{n}\times\mathrm{n}} & \\ & \boldsymbol{R}_{\mathrm{c}}(\boldsymbol{K}_{\mathrm{in}}+\boldsymbol{K}_{\mathrm{t}})\boldsymbol{R}_{\mathrm{c}}^{T}\end{bmatrix} & \begin{bmatrix}\boldsymbol{0}_{\mathrm{n}\times\mathrm{n}_{\mathrm{d}}}\\ -\boldsymbol{R}_{\mathrm{c}}\boldsymbol{K}_{\mathrm{in}}\end{bmatrix} & \begin{bmatrix}\boldsymbol{0}_{\mathrm{n}\times\mathrm{n}_{\mathrm{d}}}\\ -\boldsymbol{R}_{\mathrm{c}}\boldsymbol{K}_{\mathrm{t}}\end{bmatrix} \\ \begin{bmatrix}\boldsymbol{0}_{\mathrm{n}\times\mathrm{n}_{\mathrm{d}}} & -\boldsymbol{K}_{\mathrm{in}}\boldsymbol{R}_{\mathrm{c}}^{T}\end{bmatrix} & \boldsymbol{K}_{\mathrm{in}} & \\ \begin{bmatrix}\boldsymbol{0}_{\mathrm{n}\times\mathrm{n}_{\mathrm{d}}} & -\boldsymbol{K}_{\mathrm{t}}\boldsymbol{R}_{\mathrm{c}}^{T}\end{bmatrix} & & \boldsymbol{K}_{\mathrm{t}} \end{bmatrix} \tag{13}$$

$$[\boldsymbol{C}]=\begin{bmatrix} \boldsymbol{C}_{\mathrm{p}}^{\mathrm{c}} & & \\ & \boldsymbol{C}_{\mathrm{d}} & -\boldsymbol{C}_{\mathrm{d}} \\ & -\boldsymbol{C}_{\mathrm{d}} & \boldsymbol{C}_{\mathrm{d}} \end{bmatrix} \tag{14}$$

$$[\boldsymbol{M}_0]=\begin{bmatrix} \boldsymbol{M}_{\mathrm{p,x}}+\boldsymbol{R}_{\mathrm{c}}\boldsymbol{M}_{\mathrm{t}}\boldsymbol{R}_{\mathrm{c}}^{T} & & \\ & \boldsymbol{M}_{\mathrm{p,y}} & \\ & & \begin{matrix}\boldsymbol{M}_{\mathrm{t}} & \boldsymbol{0}_{\mathrm{n_d}\times\mathrm{n_d}}\\ \boldsymbol{0}_{\mathrm{n_d}\times\mathrm{n_d}} & \boldsymbol{0}_{\mathrm{n_d}\times\mathrm{n_d}}\end{matrix} \end{bmatrix} \tag{15}$$

$$\begin{aligned} \boldsymbol{M}_{\mathrm{t}}&=\mathrm{diag}\left(m_{\mathrm{t},1},\cdots,m_{\mathrm{t},i},\cdots,m_{\mathrm{t},\mathrm{n_d}}\right)\\ \boldsymbol{M}_{\mathrm{in}}&=\mathrm{diag}\left(m_{\mathrm{in},1},\cdots,m_{\mathrm{in},i},\cdots,m_{\mathrm{in},\mathrm{n_d}}\right)\\ \boldsymbol{K}_{\mathrm{t}}&=\mathrm{diag}\left(k_{\mathrm{t},1},\cdots,k_{\mathrm{t},i},\cdots,k_{\mathrm{t},\mathrm{n_d}}\right)\\ \boldsymbol{K}_{\mathrm{in}}&=\mathrm{diag}\left(k_{\mathrm{in},1},\cdots,k_{\mathrm{in},i},\cdots,k_{\mathrm{in},\mathrm{n_d}}\right)\\ \boldsymbol{C}_{\mathrm{d}}&=\mathrm{diag}\left(c_{\mathrm{d},1},\cdots,c_{\mathrm{d},i},\cdots,c_{\mathrm{d},\mathrm{n_d}}\right) \end{aligned} \tag{16}$$

where, $n_{\mathrm{d}}$ is the number of IeTMDs suspended from the dome. $y_{\mathrm{in}}$ and $y_{\mathrm{t}}$ are the vertical displacement vectors of the suspension masses and ball screws of IeTMDs:

$$\begin{aligned} y_{\mathrm{in}}&=\left\{y_{\mathrm{in},1},\cdots,y_{\mathrm{in},i},\cdots,y_{\mathrm{in},\mathrm{n_d}}\right\}^{T}\\ y_{\mathrm{t}}&=\left\{y_{\mathrm{t},1},\cdots,y_{\mathrm{t},i},\cdots,y_{\mathrm{t},\mathrm{n_d}}\right\}^{T} \end{aligned} \tag{17}$$

$\boldsymbol{R}_{\mathrm{c}}$ represents the suspension locations of the IeTMDs, of which different columns are related to different IeTMDs:

$$\boldsymbol{R}_{\mathrm{c}}=\begin{bmatrix} 0 & \cdots & | & 0 & | & \cdots & 0 \\ \vdots & \cdots & | & \vdots & | & \cdots & \vdots \\ \vdots & \cdots & | & 1 & | & \cdots & \vdots \\ \vdots & \cdots & | & \vdots & | & \cdots & \vdots \\ 0 & \cdots & | & 0 & | & \cdots & 0 \end{bmatrix}\begin{matrix} \\ \\ \\ \\ \\ \end{matrix}\begin{matrix} i_{\mathrm{d}} \\ \\ \\ \\ \\ \end{matrix}\begin{matrix} \\ \\ l_{\mathrm{d},i} \\ \\ \\ \end{matrix} \tag{18}$$

where, $i_{\mathrm{d}}$ is the number label of the IeTMD and $l_{\mathrm{d,i}}$ denotes the $l_{\mathrm{d,i}}$ - th IeTMD's suspension point label.

## 3. Lightweight-control-oriented design strategy

In the optimum design of the IeTMD, we should consider the weight of the suspension mass and the performance of the long-span dome simultaneously. Lightweight-control-oriented design is a design methodology where stated performance objectives are predetermined as constraints. At the same time, the weight of the additional weight is set as the design criterion to be minimized. This section introduces the performance indicators based on the direct stochastic analysis method, considering the uncertainty of the seismic excitation, and details the optimum design strategy.

### 3.1. Performance indicators

Given that the ground motion is replaced with Gaussian white noise $w(t)$, of which the mean is zero, the motion equations of the dome controlled by the IeTMDs can be rewritten as:

$$\begin{aligned} \dot{x}_{\mathrm{s}}&=\boldsymbol{A}_{\mathrm{s}}x_{\mathrm{s}}(t)+\boldsymbol{E}_{\mathrm{s}}w(t)\\ z_{\mathrm{s}}(t)&=\boldsymbol{C}_{\mathrm{s}}x_{\mathrm{s}}(t)+\boldsymbol{D}_{\mathrm{s}}w(t) \end{aligned} \tag{19}$$

where, $x_{\mathrm{s}}\in\Re^{(4\mathrm{n}+4n_{\mathrm{d}})\times1}$ is the response vector:

$$x_{\mathrm{s}}=\left\{\begin{matrix} x_{\mathrm{p}} & y_{\mathrm{p}} & y_{\mathrm{in}} & y_{\mathrm{t}} & \dot{x}_{\mathrm{p}} & \dot{y}_{\mathrm{p}} & \dot{y}_{\mathrm{in}} & \dot{y}_{\mathrm{t}} \end{matrix}\right\}^{T} \tag{20}$$

$\boldsymbol{A}_{\mathrm{s}}\in\Re^{(4\mathrm{n}+4n_{\mathrm{d}})\times(4\mathrm{n}+4n_{\mathrm{d}})}$ and $\boldsymbol{E}_{\mathrm{s}}\in\Re^{(4\mathrm{n}+4n_{\mathrm{d}})\times1}$ are the space-state matrixes:

$$\boldsymbol{A}_{\mathrm{s}}=\begin{bmatrix}\boldsymbol{0} & \boldsymbol{I}\\ -\boldsymbol{M}^{-1}\boldsymbol{K} & -\boldsymbol{M}^{-1}\boldsymbol{C}\end{bmatrix},\boldsymbol{E}_{\mathrm{s}}=\begin{bmatrix}\boldsymbol{0}_{(2\mathrm{n}+2n_{\mathrm{d}})}\\ \boldsymbol{M}^{-1}\boldsymbol{M}_0\{\widehat{\boldsymbol{r}}\}\end{bmatrix} \tag{21}$$

$z_{\mathrm{s}}$ is the space-state vector containing dynamic responses in which we are interested. $\boldsymbol{C}_{\mathrm{s}}$ is the observation matrix to define the performance indicators. $\boldsymbol{D}_{\mathrm{s}}$ is the feedforward matrix. Here, only relative displacement responses and absolute acceleration responses are considered. Thus, the system model does not have a direct feedthrough. $\boldsymbol{D}_{\mathrm{s}}$ is the zero matrix with dimensions of $2n$ times one.

By setting $\boldsymbol{C}_{\mathrm{s}}$ as follows, the nodal displacement responses relative to the ground ($x_{\mathrm{p}}$, $y_{\mathrm{p}}$) can be observed:

$$\boldsymbol{C}_{\mathrm{s}}=\boldsymbol{C}_{\mathrm{s,dis}}=\begin{bmatrix}\boldsymbol{I}_{2\mathrm{n}\times2\mathrm{n}} & \boldsymbol{0}_{2\mathrm{n_d}\times2\mathrm{n_d}}\end{bmatrix} \tag{22}$$

By setting $\boldsymbol{C}_{\mathrm{s}}$ as follows, absolute acceleration responses can be observed:

$$\boldsymbol{C}_{\mathrm{s}}=\boldsymbol{C}_{\mathrm{s,acc}}=\begin{bmatrix}-\boldsymbol{M}^{-1}\boldsymbol{K} & -\boldsymbol{M}^{-1}\boldsymbol{C}\end{bmatrix} \tag{23}$$

By resolving the following Lyapunov equation, it is possible to determine the root-mean-square (RMS) seismic space-state responses of the dome under the control of the IeTMD [56]:

$$\boldsymbol{A}_{\mathrm{s}}\boldsymbol{S}+\boldsymbol{S}\boldsymbol{A}_{\mathrm{s}}^{T}+\boldsymbol{E}_{\mathrm{s}}\boldsymbol{E}_{\mathrm{s}}^{T}=0 \tag{24}$$

Thus, a comprehensive performance indicator can be defined as:

$$\sigma_{\mathrm{p}}=\sum_{j=1}^{2n}\rho_j^{\mathrm{dis}}\sqrt{\boldsymbol{C}_{\mathrm{s,dis}}\boldsymbol{S}(j,j)\boldsymbol{C}_{\mathrm{s,dis}}^{T}}+\sum_{j=1}^{2n}\rho_j^{\mathrm{acc}}\sqrt{\boldsymbol{C}_{\mathrm{s,acc}}\boldsymbol{S}(j,j)\boldsymbol{C}_{\mathrm{s,acc}}^{T}} \tag{25}$$

Importance coefficients $\rho_j^{\mathrm{dis}}$ and $\rho_j^{\mathrm{acc}}$ denote the significance of each node's displacement and acceleration, respectively. They satisfy the following relationships:

$$\sum_{j=1}^{2\mathrm{n}}\rho_j^{\mathrm{dis}}+\sum_{j=1}^{2\mathrm{n}}\rho_j^{\mathrm{acc}}=1 \tag{26}$$

Set $\rho_j^{\mathrm{dis}}\equiv0$, the indicator in (25) represent the acceleration performance. Similarly, set $\rho_j^{\mathrm{acc}}\equiv0$, the indicator in (25) represent the displacement performance.

### 3.2. Optimum design strategy

Based on the performance indicators in Eq. (25), a dimensionless mitigation ratio can be defined for formulating the optimal problem:

$$\gamma_{\mathrm{P}}=\frac{\sigma_{\mathrm{p}}}{\sigma_{\mathrm{p,0}}} \tag{27}$$

where, $\sigma_{\mathrm{p,0}}$ is the uncontrolled dome's performance indicator.

The following five dimensionless parameters are used to simplify the IeTMD optimization expression and subsequent parametric investigation.

$$\mu_{\mathrm{t}}=\frac{m_{\mathrm{t}}}{M_0},\kappa_{\mathrm{t}}=\frac{k_{\mathrm{t}}}{M_0\omega_0^2},\xi_{\mathrm{in}}=\frac{c_{\mathrm{in}}}{2M_0\omega_0},\kappa_{\mathrm{in}}=\frac{k_{\mathrm{in}}}{M_0\omega_0^2},\mu_{\mathrm{in}}=\frac{m_{\mathrm{in}}}{m_{\mathrm{t}}} \tag{28}$$

where, $M_0$ is the total mass of the uncontrolled half-dome. $\omega_0$ is the natural frequency of the dome. $\mu_{\mathrm{t}}$ is the suspension mass ratio. $\kappa_{\mathrm{t}}$ and $\kappa_{\mathrm{in}}$ are the stiffness ratios of the spring used to tune the suspension mass and the TVMD-like substructure, respectively. $\mu_{\mathrm{in}}$ is the inertia-mass ratio.

Then, the design of the IeTMD can be expressed as a numerical optimization problem:

$$\begin{aligned} &\underset{\nu\in V}{\text{minimize}} && \mu_t \\ &s.t. && \gamma_P(\nu)\leqslant\gamma_{P,\text{demand}} \end{aligned} \tag{29}$$

where, $\nu=\{\mu_{in},\mu_t,\kappa_t,\kappa_{in},\xi_{in}\}$ is a vector of design variables and $V$ is the feasibility domain.

$$V=\begin{cases} \mu_{in,min}\leqslant\mu_{in}\leqslant\mu_{in,max} \\ \mu_{t,min}\leqslant\mu_t\leqslant\mu_{t,max} \\ \kappa_{t,min}\leqslant\kappa_t\leqslant\kappa_{t,max} \\ \kappa_{in,min}\leqslant\kappa_{in}\leqslant\kappa_{in,max} \\ \xi_{in,min}\leqslant\xi_{in}\leqslant\xi_{in,max} \end{cases} \tag{30}$$

In function (30), $\mu_{in,min}$, $\mu_{t,min}$, $\kappa_{t,min}$, $\kappa_{in,min}$, and $\xi_{in,min}$ denote the lower bounds of design variables, while $\mu_{in,max}$, $\mu_{t,max}$, $\kappa_{t,max}$, $\kappa_{in,max}$, and $\xi_{in,max}$ denote the upper bounds.

Hence, the flowchart is depicted in Fig. 3. The lightweight-control-oriented design procedure can be concluded as follows:

Step 1: Perform modal analysis of the uncontrolled primary dome to obtain its natural frequencies and modal shapes. Solve the specific Lyapunov equation of the uncontrolled primary dome to get the performance indicator defined in Section 3.1, quantifying the performance of a dome subjected to ground motion excitations.

Step 2: Based on the analysis results in Step 1, choose the suspension points to install the IeTMD and determine the target mitigation ratio $\gamma_{P,\text{demand}}$ according to the performance demand.

Step 3: Substitute the stated target mitigation ratio $\gamma_{P,\text{demand}}$ into Eq. (29) to establish a numerical optimization problem for designing IeTMD.

Step 4: Solve the optimization problem (Eq. (29)) to determine the vector of design variables $\nu=\{\mu_{in},\mu_t,\kappa_t,\kappa_{in},\xi_{in}\}$.

Step 5: Verify the performance of the controlled dome and the lightweight effect of IeTMD.

## 4. Lightweight performance of IeTMD for long-span dome

In this section, parametric analysis is carried out to illustrate the degree to which IeTMD can improve the performance of the long-span dome when its key parameters (i.e., $\mu_{in}$, $\kappa_t$, $\kappa_{in}$, and $\xi_{in}$) change within certain ranges. Meanwhile, the lightweight performance of the IeTMD is also investigated by comparing it to an associated TMD with the same suspension mass ($k_{in}=\infty$, $m_{in}=0$). The target benchmark is set as the dome to be investigated, for which the total mass of the half dome is 39000 kg. The natural frequency is 6.754 rad/s.

### 4.1. Performance improvement from the IeTMD

First, as a particular case of the IeTMD in a limit state ($k_{in}=\infty$, $m_{in}=0$), equivalent to a TMD (called an associated TMD), the effect of key parameters ($\mu_t$, $\kappa_t$, and $\xi_t=\xi_{in}$) on the control performance is tested, where $\mu_t$ equals 0.01, 0.02, 0.10, and 0.20; $\xi_t$ continuously changes from $10^{-5}$ to $10^{-2}$; $\kappa_t$ continuously changes from $10^{-2}$ to $10^{0}$. Fig. 4 depicts the results in the form of contour plots, where $\xi_t$ and $\kappa_t$ are represented on logarithmic scales. As expected, with the help of a well-designed associated TMD, the performance of the long-span dome is improved ($\gamma_P<1$). A significant decrease in $\gamma_p$ accompanies an increase in $\mu_t$, while the increment rate decreases. Valley topologies always exist in the contour plots for different suspension mass ratios ($\mu_t$), of which the lowest points are marked with red dots. This ensures the optimization solution's validity within the parameters' scope. In addition, the contours show that the reduction in the mitigation ratio is insignificant when the parameter is varied in the direction of the damping ratio (the red arrow's direction). In contrast, the opposite conclusion is reached when it is varied in the direction of the stiffness ratio $\kappa_t$. It means the effectiveness of the TMD is robust to damping deviations while being highly dependent on the tuning quality and sensitive to the variation of tuning parameters.

Furthermore, Figs. 5 and 6 illustrate the influence of critical parameters (i.e., $\mu_{in}$, $\kappa_{in}$, and $\xi_{in}$) that differ from those in associated TMD on mitigating seismic responses. The suspension mass ratio $\mu_t$ and tuning stiffness ratio $\kappa_t$ are predetermined according to the parametric analysis for the associated TMD. For the sake of simplicity, only a small number of discrete inertia-mass ratios $\mu_{in}$ (0.04, 0.05, 0.06, and 0.10 for $\mu_t=0.01$, and 0.04, 0.05, 0.06, and 0.10 for $\mu_t=0.10$) are shown in Figs. 5 and 6 to illustrate the changing trend in mitigation ratio $\gamma_p$ with $\mu_{in}$. The damping ratio $\xi_{in}$ continuously changes from $10^{-5}$ to $10^{-2}$, and the stiffness ratio $\kappa_{in}$ continuously changes from $10^{-2}$ to $10^{0}$. As shown in Fig. 5 and Fig. 6, red planes denote the best control performances of associated TMDs. The white boxes enclose parameter ranges within which the IeTMD maintains a more excellent vibration control performance than the associated TMD.

The mitigation ratio of the IeTMD tends to decrease and then increase as the inertia-mass ratio increases. It implies that, for a given $\mu_t$, an optimal $\mu_{in}$ exists in a valley bottom such that the IeTMD obtains the most excellent damping effect. As depicted in Fig. 5(b) and Fig. 6(c), the optimal $\mu_{in}$ for $\mu_t=0.01$ and $\mu_t=0.10$ are 0.02 and 0.06, respectively.

Notably, each contour plot in Figs. 5 and 6 demonstrates that the enclosed regions can be approximately divided into two categories (Regions A and B). The white arrow designates Region A, where the control performance of IeTMD fluctuates less with the stiffness ratio $\kappa_{in}$. Meanwhile, the range of the damping ratio $\xi_{in}$ in Region A is close to the optimal damping ratio $\xi_t$ of the associated TMD. It means that in Region A, the resonance of the TVMD-like substructure is suppressed under the influence of the large stiffness ratio $\kappa_{in}$, and the IeTMD almost metamorphoses into an associated TMD. On the other hand, a yellow arrow indicates Region B, where IeTMD can achieve its best damping performance with less damping and stiffness needed. In this region, the performance of the IeTMD is robust to changes in the damping ratio $\xi_{in}$ and sensitive to the tuning stiffness ratio $\kappa_{in}$. It is consistent with the need for

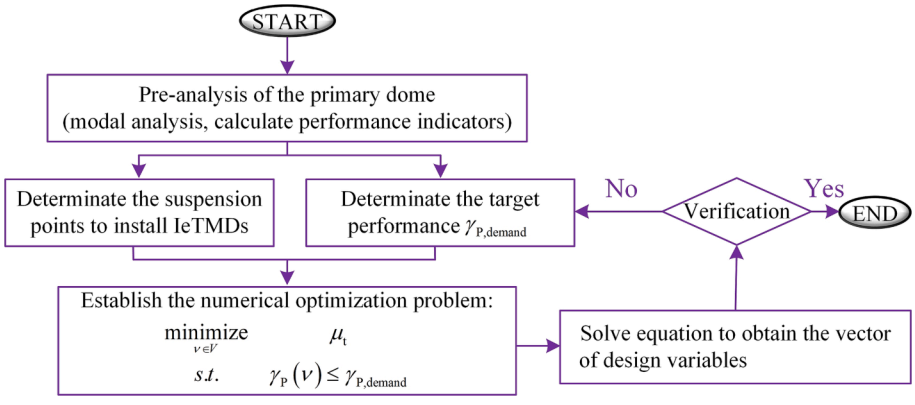


**Fig. 3.** Design flowchart for the lightweight-control-oriented design of IeTMD.

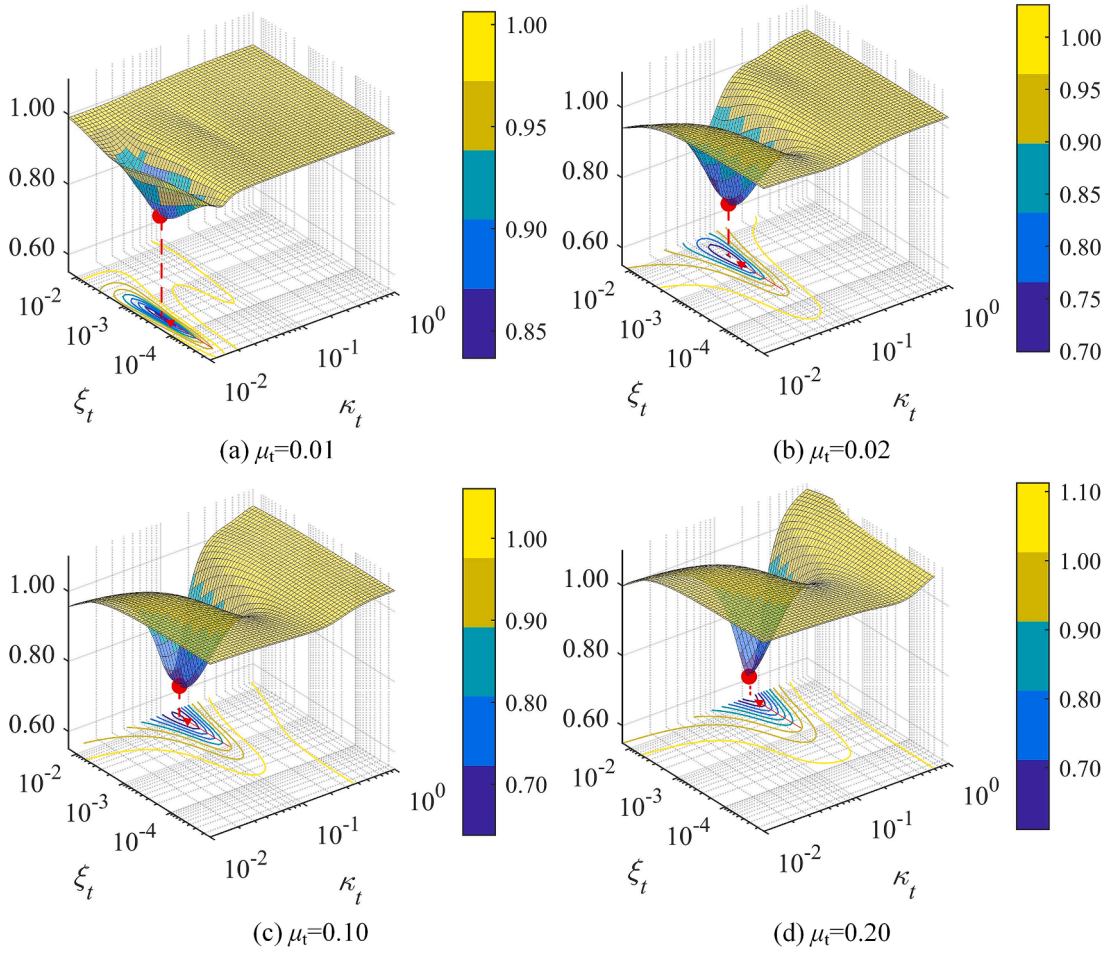


**Fig. 4.** Contour plots of control performance for TMDs ($\kappa_{in} = \infty$, $\mu_{in} = 0$).

resonance in the TVMD-like substructure, indicating that a well-designed IeTMD with its stiffness and damping parameters located in Region B can obtain the effective mitigation and damping enhancement effect shown in Fig. 7. In Fig. 7, the index is the damping enhancement factor $\gamma_d$.

$$\gamma_d = \frac{\sigma^{dis}_{damper}}{\sigma^{dis}_{IeTMD}} \tag{31}$$

where, $\sigma^{dis}_{damper}$ is the RMS relative displacement of the damping element; $\sigma^{dis}_{IeTMD}$ is the RMS displacement of the IeTMD.

### 4.2. Quantified lightweight control effect

To further quantify the lightweight control effect of the IeTMD, the following mass reduction ratio $\alpha_\mu$ is defined herein:

$$\alpha_\mu = \frac{\mu_{t,TMD} - \mu_{t,IeTMD}}{\mu_{t,TMD}} \times 100\% \tag{32}$$

where, $\mu_{t,TMD}$ and $\mu_{t,IeTMD}$ are the suspension mass ratios of the TMD and IeTMD designed for the same target performance, respectively.

Table 1 lists the suspension mass ratios $\mu_{t,IeTMD}$ and corresponding mass reduction ratios $\alpha_\mu$ for IeTMD designed based on the lightweight-control-oriented design procedure for six target performances ($\gamma_{P,demand}$=0.55–0.80). It can be observed that IeTMD with a lighter suspension mass can achieve the same control effect as TMD. The mass reduction ratios ($\alpha_\mu$) reach around 20 %. Since the suspension mass is strictly limited to be suspended from a long-span dome (typically, $\mu_t$ is selected less than 0.10 in practice [24]), around 20 % mass reduction is vital for the seismic response control of the dome. In other words, considering the suspension mass limitation for the long-span dome in practice, with the help of a lightweight effect, IeTMD can obtain a better vibration mitigation effect than TMD, as shown in Fig. 8.

Observing the optimized distributions of $\mu_t$, $\kappa_t$, $\kappa_{in}$, $\xi_{in}$, and $\mu_{in}$ reveals a clear trend: as the target performance index $\gamma_{P,demand}$ increases, parameters $\mu_t$, $\kappa_t$, $\kappa_{in}$, $\xi_{in}$, and $\mu_{in}$ consistently decrease. To achieve initial practical parameters for the IeTMD, empirical design formulae for $\mu_t$, $\kappa_t$, $\kappa_{in}$, $\xi_{in}$, and $\mu_{in}$, with respect to the target performance index $\gamma_{P,demand}$, are fitted. After assessing different equation forms through the fitting procedure described in [57], we selected Eqs. (33) to (37) to strike a balance between accuracy and ease of use.

$$\mu_t = \exp\left[A_1 + A_2\gamma_{p,demand} + A_3\gamma^{-1}_{p,demand}\right] \tag{33}$$

$$\kappa_t = \exp\left[B_1 + B_2\gamma_{p,demand} + B_3\gamma^{-1}_{p,demand}\right] \tag{34}$$

$$\kappa_{in} = \exp\left[C_1 + C_2\gamma_{p,demand} + C_3\gamma^{-1}_{p,demand}\right] \tag{35}$$

$$\xi_{in} = \exp\left[D_1 + D_2\gamma_{p,demand} + D_3\gamma^{-1}_{p,demand}\right] \tag{36}$$

$$\mu_{in} = \exp\left[E_1 + E_2\gamma_{p,demand} + E_3\gamma^{-1}_{p,demand}\right] \tag{37}$$

The values of the coefficients $A_j$, $B_j$, $C_j$, and $D_j$ (j = 1, 2, 3) are listed in Table 2. As shown in Fig. 9, The values of $\mu_t$, $\kappa_t$, $\kappa_{in}$, $\xi_{in}$, and $\mu_{in}$ calculated using Eqs. (33) to (37) agree well with the optimal parameters obtained

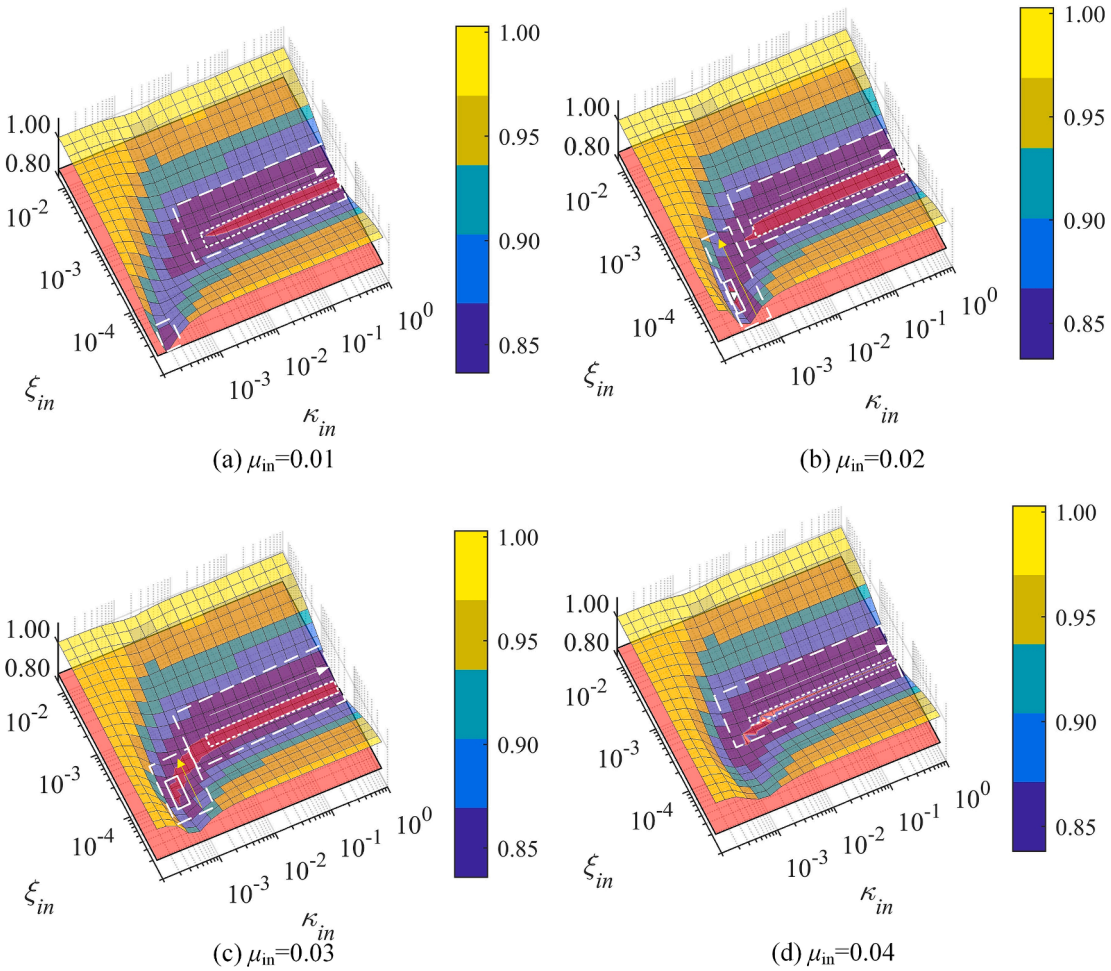


**Fig. 5.** Contour plots of control performance of the long-span domes with IeTMDs and TMDs for suspension mass ratio ($\mu_t = 0.010$, $\kappa_t = 0.014$).

through the lightweight-control-oriented design procedure proposed in this study, correspondingly stressing the significance of the fitted design formulae.

### 4.3. Case design and illustration

The dimensions of the benchmark dome structure [24] are listed in Table 3. The Young's modulus of the material is $2.05\times10^5$N/mm$^2$. The cross-sectional areas of the arch beams and column legs are $5.38\times10^4$ mm$^2$ and $5.89\times10^4$ mm$^2$, respectively. The section's second moments of the arch beam and column leg are $1.18\times10^{10}$ mm$^4$ and $1.35\times10^{10}$ mm$^4$, respectively. The number of the dome's discrete nodes is 13 (n = 13). Each node on the arch beam has a concentrated mass of 6000 kg, representing 976 kg of mass per unit length of the arch beam. The inherent damping is assumed to be Rayleigh type, with the first and second damping ratios equaling 2 % [55].

Following the lightweight-control-oriented design flowchart, IeTMDs are designed to control the benchmark dome's seismic responses.

*Step 1: Perform modal analysis of the uncontrolled primary dome.*

Fig. 10 depicts the modal analysis results of the benchmark dome. The frequencies of the first-order, second-order, third-order, and fourth-order modes are 6.754 rad/s, 7.938 rad/s, 17.277 rad/s, and 28.309 rad/s, respectively. The frequency response functions of the vertical displacements of the benchmark dome are illustrated in Fig. 11, where blue vertical lines mark the frequencies of the dome. It shows that the second-order mode is the dominant vertical vibration mode. The larger vertical displacements occur at Nodes 4 and 10.

*Step 2: Choose the suspension points to install the IeTMD and determine the target mitigation ratio $\gamma_{P,demand}$.*

Based on the analysis results in Step 1, Nodes 4 and 10 are selected as suspension points. In sets $\rho_j^{dis} = \frac{1}{13}, (j = 2, 4, \cdots 26)$ and $\rho_j^{acc} \equiv 0$, the performance indicator represents the sum of each node's vertical RMS displacement. According to Eq. (25), the uncontrolled performance indicator $\sigma_{p,0}$ can be obtained, equaling 0.0611. To reduce the seismic responses, for example, the IeTMD is designed with a target mitigation ratio of $\gamma_{P,demand} = 0.616$.

*Step 3: Establish a numerical optimization problem.*

Substituting$\gamma_{P,demand} = 0.616$ into Eq. (29), the numerical optimization problem of the IeTMD can be established as:

$$\begin{aligned} &\underset{\nu\in V}{\text{minimize}} && \mu_t \\ &s.t. && \gamma_P(\nu) \leqslant 0.616 \end{aligned} \tag{38}$$

*Step 4: Solve the optimization problem (Eq. (29)) or directly use the empirical design formulae (33) to (37).*

The vector of design variables $\nu = \{\mu_{in}, \mu_t, \kappa_t, \kappa_{in}, \xi_{in}\}$ can be obtained:

$$\nu^o = \left\{5.21\times10^{-2}, 1.00\times10^{-1}, 1.25\times10^{-1}, 7.1\times10^{-3}, 8.4295\times10^{-4}\right\} \tag{39}$$

where, the upper script 'o' denotes the optimal result. Applying the numerical method in MATLAB [58] to solve the optimization problem (Eq. (29)) yields the optimal design parameters, shown as blue circles in Fig. 9. These outcomes are consistent with empirical and simplified design formulas.

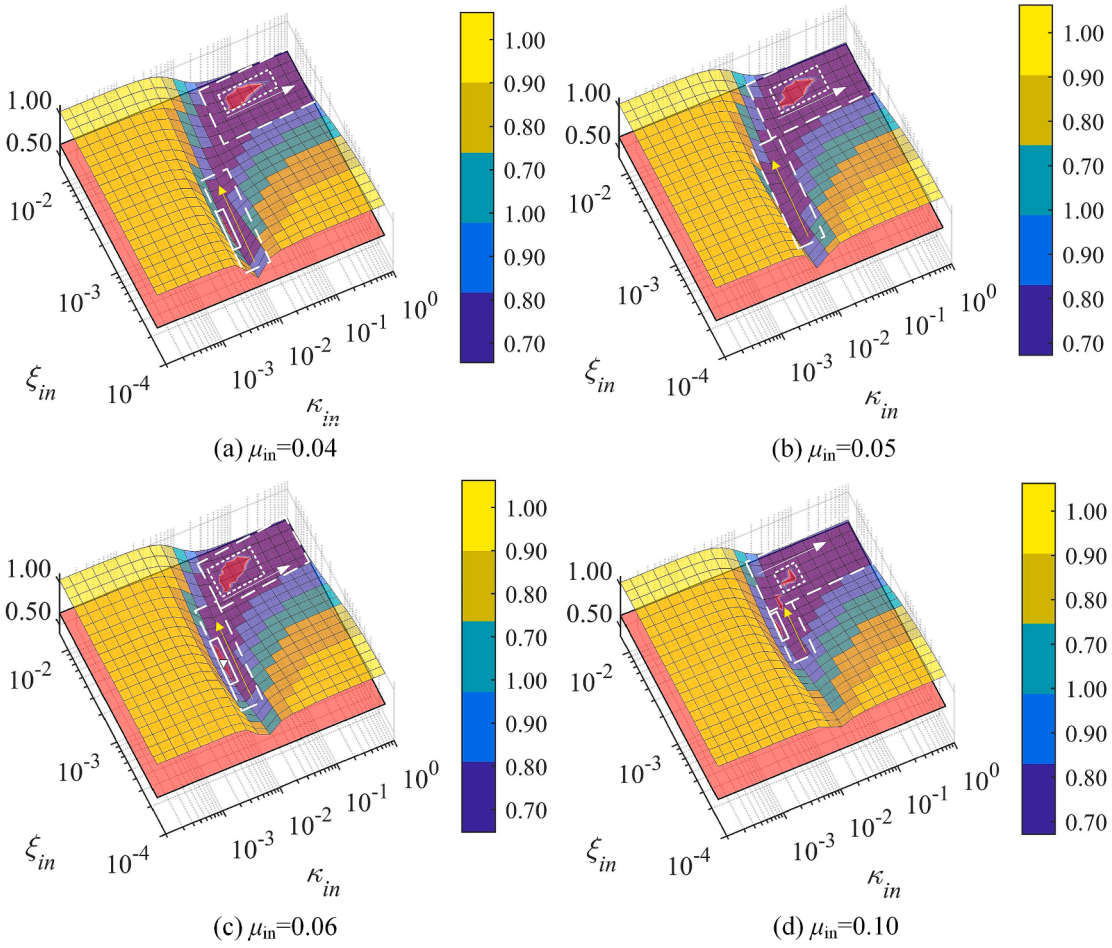


**Fig. 6.** Contour plots of control performance of the long-span domes with IeTMDs and TMDs for suspension mass ratio ($\mu_t = 0.100$, $\kappa_t = 0.130$).

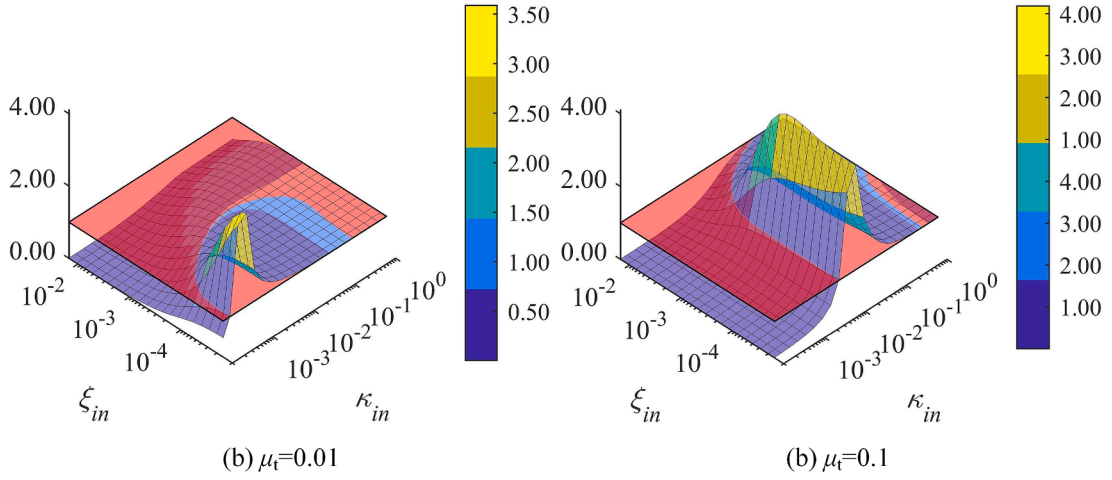


**Fig. 7.** Contour plots of the damping enhancement effect of the IeTMDs.

Thus, the apparent mass $m_{in}$, the suspension mass $m_t$, tuning spring $k_t$ and $k_{in}$, and damping coefficient $c_{in}$ of each IeTMD are 101.60 kg, 1950.00 kg, 111457.11 N/m, 6315.61 N/m, and 222.04 N·s/m, respectively.

*4.3.1. Seismic response mitigation effect*

In this section, the seismic response mitigation effect of the designed IeTMD with the parameters in Eq. (39) is verified with a series of time history analyses. Three recorded earthquake accelerograms, including the Taft accelerogram (1952), the Hector Mine accelerogram (1999), and the Loma Prieta accelerogram (1989), are used. The peak ground accelerations of these three recorded earthquake accelerograms are scaled to 0.1 g. The time history analysis results, in terms of the horizontal and vertical displacements, horizontal and vertical accelerations, and base shear, are depicted in Figs. 12 and 13 as examples subjected to the Loma Prieta accelerogram. The displacements of the IeTMD and its

**Table 1**
Suspension masses of the IeTMD and TMD for different performance requirements.

| Target performance $\gamma_{p,\,demand}$ | TMD ($\mu_t$) | IeTMD ($\mu_t$) | $\alpha_\mu$ (%) |
|---|---|---|---|
| 0.55 | 0.337 | 0.275 | 18.98 |
| 0.60 | 0.157 | 0.116 | 26.22 |
| 0.65 | 0.087 | 0.065 | 24.86 |
| 0.70 | 0.049 | 0.035 | 26.80 |
| 0.75 | 0.028 | 0.022 | 21.82 |
| 0.80 | 0.016 | 0.012 | 22.58 |

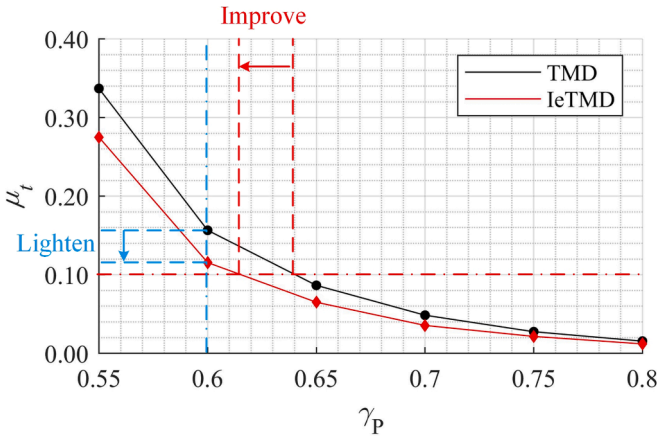


**Fig. 8.** Relationship between the suspension mass ratios and the performance index.

**Table 2**
Values of coefficients in the empirical design formulae for $\mu_t$, $\kappa_t$, $\kappa_{in}$, $\xi_{in}$, and $\mu_{in}$.

| Coefficient | $j=1$ | $j=2$ | $j=3$ |
|---|---|---|---|
| $A_j$ | −6.257 | −3.595 | 3.797 |
| $B_j$ | −3.804 | −4.855 | 2.893 |
| $C_j$ | −13.099 | −6.056 | 7.284 |
| $D_j$ | −10.164 | −12.711 | 6.706 |
| $E_j$ | −4.403 | −4.534 | 2.596 |

damping element are illustrated in Fig. 14. Meanwhile, Fig. 15 plots the hysteretic curve of the damping element in the IeTMD.

Within each time history analysis subgraphs, we have marked the peak values of displacement and acceleration responses. Specifically, $D_{un}$ and $D_{con}$ denote the peak values of uncontrolled and controlled displacement responses, respectively, while $A_{un}$ and $A_{con}$ correspond to the respective peak acceleration values. The left subscript '$j$' signifies the node's index, and the right superscript 'x' or 'y' indicates the direction. Meanwhile, the mitigation ratios defined in the time domain are marked in Fig. 12 to represent the response mitigation effect:

$$ {}_j\gamma^x_{p,dis} = \frac{\sigma^x_{IeTMD,dis}}{\sigma^x_{0,dis}},\ {}_j\gamma^y_{p,dis} = \frac{\sigma^y_{IeTMD,dis}}{\sigma^y_{0,dis}},\ {}_j\gamma^x_{p,acc} = \frac{\sigma^x_{IeTMD,acc}}{\sigma^x_{0,acc}},\ {}_j\gamma^y_{p,acc} = \frac{\sigma^y_{IeTMD,acc}}{\sigma^y_{0,acc}} \tag{40}$$

where, $\sigma^x_{0,dis}$, $\sigma^y_{0,dis}$, $\sigma^x_{0,acc}$, and $\sigma^y_{0,acc}$ denote the RMS responses of the uncontrolled dome in terms of the bi-direction displacements and bi-direction accelerations, respectively. $\sigma^x_{0,dis}$, $\sigma^y_{0,dis}$, $\sigma^x_{0,acc}$, and $\sigma^y_{0,acc}$ denote the RMS responses of the IeTMD-controlled dome.

The mitigation ratios indicate that IeTMD provides efficient control of the displacement and acceleration responses of each node of the dome. Meanwhile, the average mitigation ratios for three selected recorded earthquake accelerograms in Table 4 show that the target mitigation ratio has been ensured ($0.6112 < \gamma_{P,demand}$). In addition, the

**Table 3**
The dimensions of the benchmark dome.

| Column height $H$ (m) | Rise $h$ (m) | Span $L$ (m) | Radius $R$ (m) | half subtended angle $\theta$ (deg) |
|---|---|---|---|---|
| 15.0 | 5.20 | 79.0 | 152.6 | 15.0° |

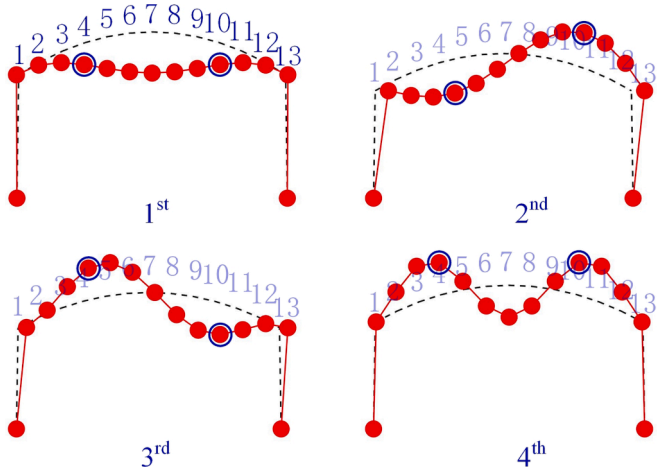


**Fig. 10.** Modal analysis results of the benchmark dome.

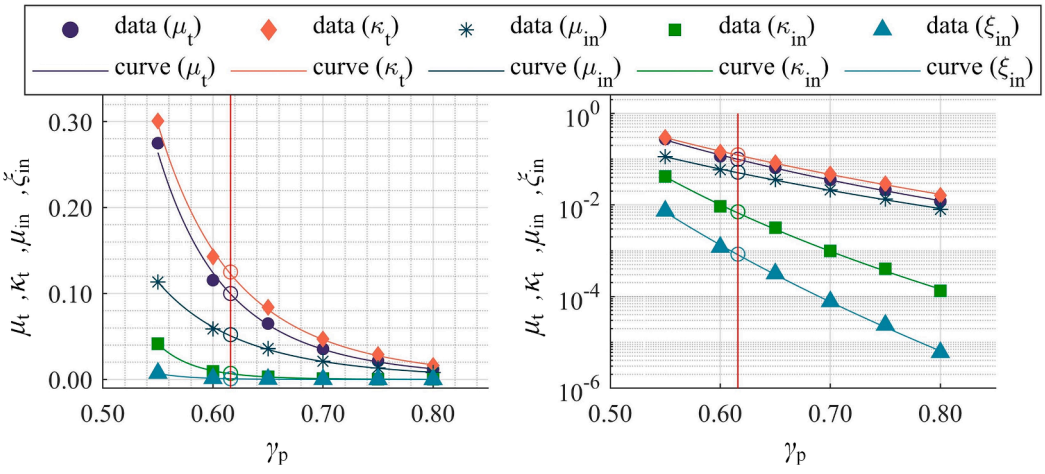


**Fig. 9.** Curves of the empirical design formulae for $\mu_t$, $\kappa_t$, $\kappa_{in}$, $\xi_{in}$, and $\mu_{in}$.

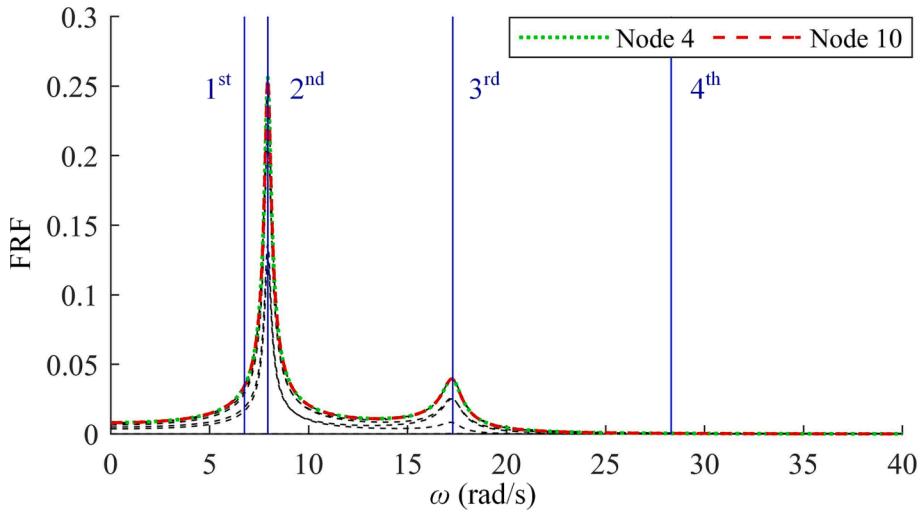


**Fig. 11.** Frequency response functions (FRFs) of the benchmark dome (y-dir).

time history results in Figs. 12 and 13 show that IeTMD has a relatively poor control effect during the early excitation stage. It means that IeTMD requires a certain amount of start time to mitigate the seismic responses efficiently, consistent with typical tuned-type vibration control devices. [59,60]. In Fig. 14, the overall deformation response is obtained by combining the results of time history analysis from various points and superimposing the dynamic displacements onto the initial structural shapes of both controlled and uncontrolled domes. To enhance clarity, the deformations have been magnified by a factor of 1000. Notably, a strong correlation between horizontal and vertical deformations in the dome is evident [5]. When IeTMDs are vertically suspended, both horizontal and vertical deformations in the long-span dome experience significant reduction.

Fig. 15 shows that the relative displacement of the damping element is much larger than that of the IeTMD under the Loma Prieta earthquake. To quantify this displacement amplification effect, a damping enhancement factor $\gamma_d$ is also marked in Fig. 15.

The damping enhancement factors for the Taft accelerogram, the Hector Mine accelerogram, and the Loma Prieta accelerogram are 3.03, 2.97, and 3.01, respectively, which are all much larger than units. It means that the vibration energy dissipated by the damping element is larger compared with a single damping element.

Meanwhile, the hysteretic curves of damping elements in the IeTMD and associated TMD are depicted simultaneously in Fig. 16. The associated TMD has the same suspension mass as IeTMD, and its tuning stiffness and damping coefficient are optimized ($k_t$=113591.96 N/m, $c_t$=2528.69 N·s/m). It can be observed that although the displacements of the IeTMD and TMD are similar, the damping element in the IeTMD is still effective in dissipating energy with the help of resonance within the TVMD-like substructure.

#### 4.3.2. *Performance improvement*

Hence, in this section, the performance improvement of the IeTMD compared to the associated TMD is verified through frequency domain analysis and time history analysis. The suspension mass of the associated TMD is the same as the IeTMD. The optimal damping coefficient $c_t$ and tuning stiffness $k_t$ of each TMD are 2528.69 N·s/m and 113591.97 N/m, respectively. The mitigation ratio $\gamma_p$ of the associated TMD calculated based on the stochastic vibration analysis is 0.638. It indicates that the IeTMD, of which the mitigation ratio $\gamma_p$ is 0.616, can control the dome more efficiently than the associated TMD.

The normalized FRFs of the controlled and uncontrolled domes in Fig. 17 indicate that employing the IeTMD results in a seismic response approximately 17 % lower in terms of $H\infty$ compared to using the corresponding TMD. It is evident that the IeTMD, featuring an additional TVMD-like substructure, exhibits a distinct response characteristic compared to the associated TMD. Specifically, the designed IeTMD, operating as a two-degree-of-freedom system, possesses two closely spaced natural frequencies at 6.860 rad/s and 8.689 rad/s. These two frequencies are positioned on either side of the target control modal frequency of 7.938 rad/s. This implies that, in contrast to the associated TMD with a single natural frequency of 7.632 rad/s, the IeTMD, similar to the spatially dispersed multiple TMDs mentioned in [25], can effectively resonate with the long-span dome in the vicinity of frequencies 6.860 rad/s and 8.689 rad/s, resulting in a broader control bandwidth. Quantitatively, the control bandwidth of IeTMD is 1.58 times that of TMD.

Furthermore, Fig. 18 illustrates normalized FRFs for the suspension mass and damper of the IeTMD and TMD, indicating that the damper element's displacement responses of the IeTMD are significantly higher than those of the TMD through resonance. It guarantees that IeTMD can achieve better control performance even with only 8.78 % of the damping coefficient required for TMD. Fig. 19 compares the time history responses of the dome controlled by IeTMDs and TMDs subjected to the Loma Prieta accelerogram, where $\alpha_\gamma$ denotes the performance improvement of the IeTMD compared with the TMD.

$$\alpha_\gamma = \frac{\gamma_p^{\mathrm{TMD}} - \gamma_p^{\mathrm{IeTMD}}}{\gamma_p^{\mathrm{IeTMD}}} \times 100\% \tag{41}$$

where, $\gamma_p^{\mathrm{IeTMD}}$ and $\gamma_p^{\mathrm{TMD}}$ are the mitigation ratios of the IeTMD and the TMD.

The average $\alpha_\gamma$ for the selected three earthquakes is listed in Table 5. Fig. 20 shows that the dominant response frequencies of the controlled structure are mostly spread between the two peaks of the FRF of the long-span dome controlled by the IeTMD (6.8–8.2 rad/s, marked as green dotted lines) shown in Fig. 17. In addition, the wavelet transforms reveal that the response frequency coincides with the transition region between the valley of the TMD and the intermediate peak of the IeTMD (7.5–8.0 rad/s, marked as red dotted lines) for the Taft accelerogram case. As depicted in Fig. 17, the control efficacy of the IeTMD is slightly inferior to that of the TMD in this region. As a result, when compared to the Hector Mine accelerogram and Loma Prieta accelerogram, the IeTMD's performance improvement efficacy is slightly lower than the TMD's (measured by $\alpha_\gamma$). Taking the stochastic nature of earthquakes into consideration, the performance improvement of the IeTMD varies with the earthquake, while the average $\alpha_\gamma$ of 9.00 % indicates that with the same suspension mass constraint, the IeTMD proposed herein can achieve better control performance than the TMD.

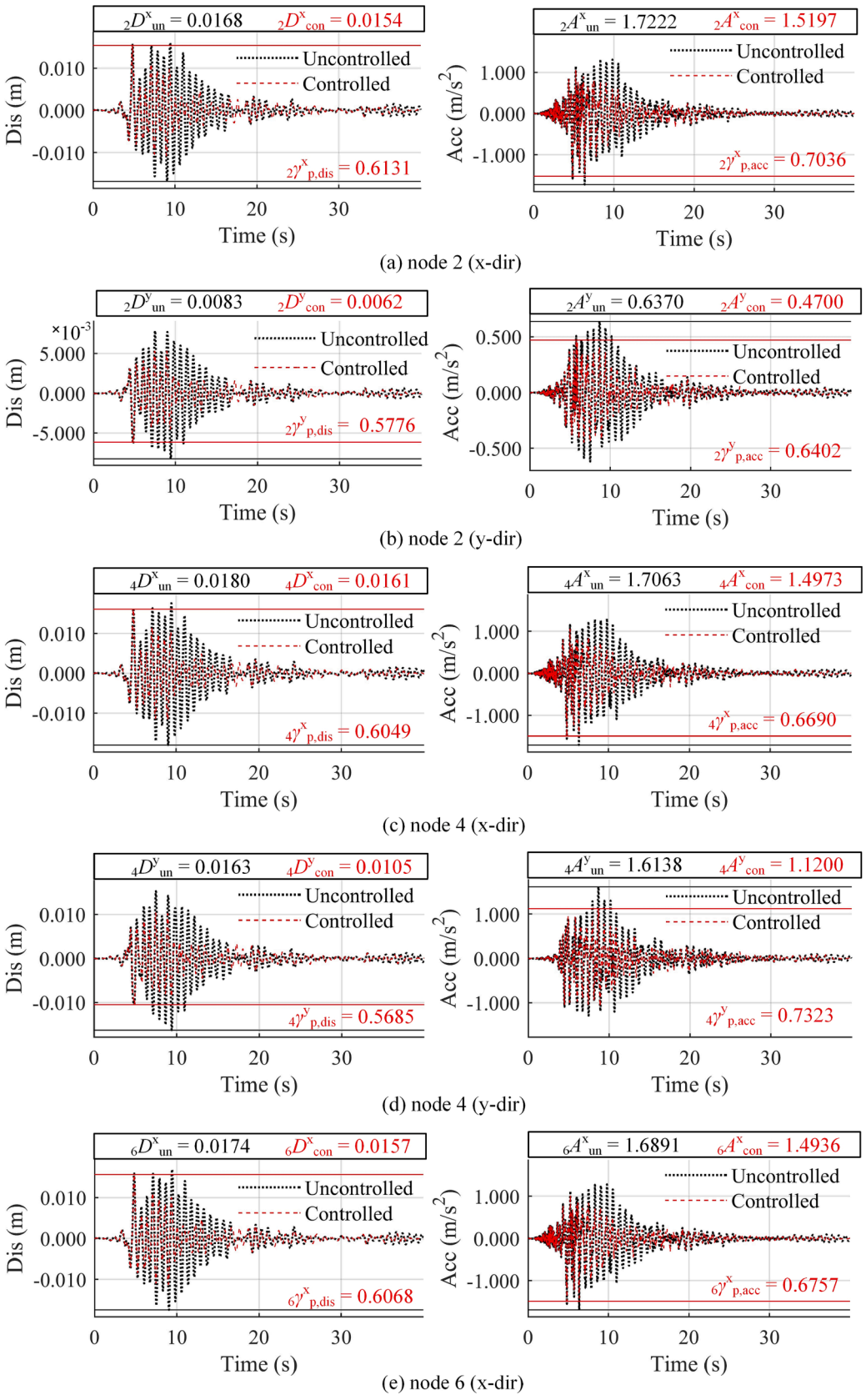


**Fig. 12.** Displacement and acceleration responses of the controlled and uncontrolled domes.

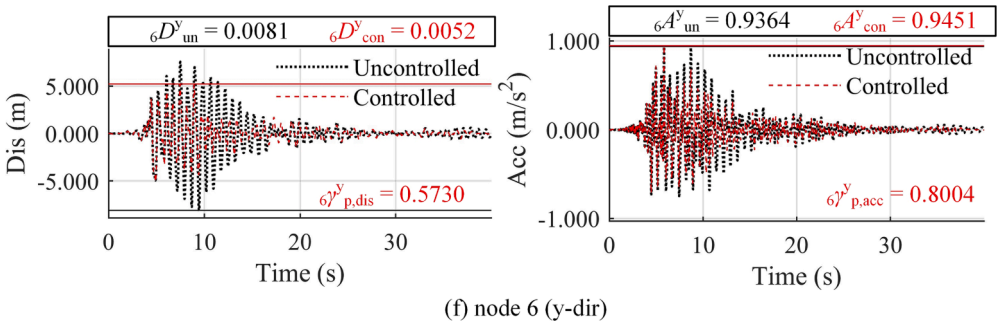


(f) node 6 (y-dir)

**Fig. 12.** (*continued*).

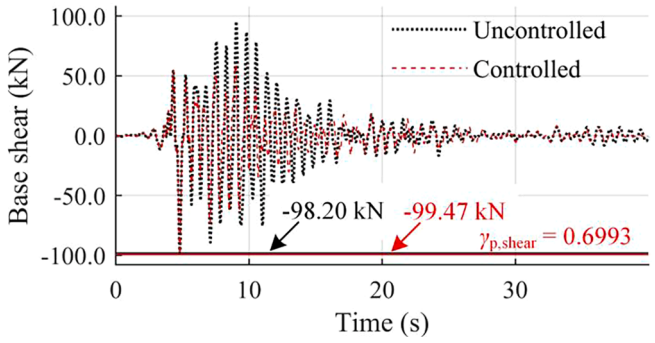


**Fig. 13.** Base shear responses of the controlled and uncontrolled domes.

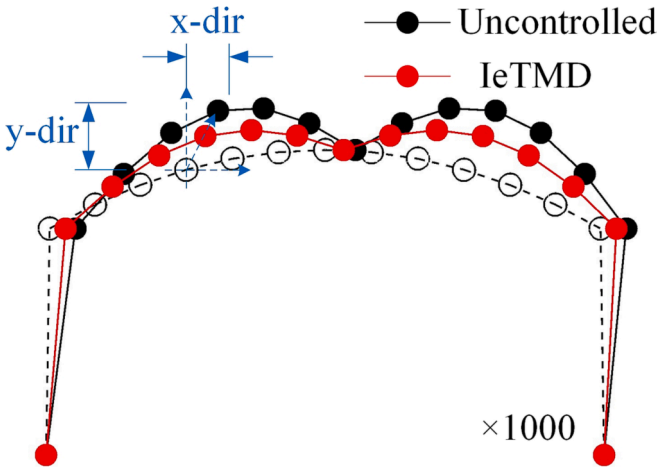


**Fig. 14.** Overall deformation responses of the controlled and uncontrolled domes.

#### 4.3.3. *Bi-directional seismic effect*

As an extension of the preceding discussion, this section delves further into the influence of bi-directional seismic motion on the performance of IeTMDs. Utilizing the Loma Prieta accelerogram as an illustrative example, Fig. 21 illustrates the time history responses of displacement and acceleration at a representative node (Node 4) for both controlled and uncontrolled domes subjected to bi-directional seismic input. It is evident that the vertical response of the long-span dome significantly increases due to the vertical seismic motion. When compared to the scenario with only horizontal seismic input, the maximum vertical displacement at Node 4 in the uncontrolled structure increases from 0.01163 m to 0.0188 m, and the acceleration increases from 1.6138 m/s$^2$ to 1.9628 m/s$^2$. Table 6 lists the mitigation ratios of the dome controlled by designed IeTMDs considering horizontal and bi-directional seismic excitations. Notably, although the damping performance of designed IeTMDs experiences a slight reduction under bi-directional seismic motion, particularly in terms of vertical displacement reduction, their damping effectiveness remains acceptable.

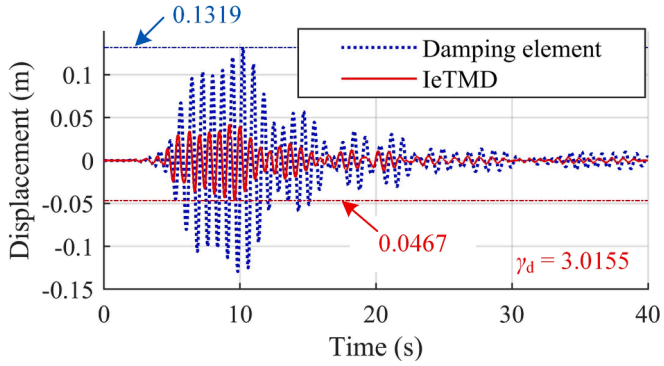


**Fig. 15.** Relative displacement of the damping element and the IeTMD.

**Table 4**
Mitigation ratios of the dome controlled by designed IeTMDs.

| Ground motion | $\gamma^x_{p,dis}$ | $\gamma^y_{p,dis}$ | $\gamma^x_{p,acc}$ | $\gamma^y_{p,acc}$ | $\gamma_{p,shear}$ | $\gamma_d$ |
|---|---|---|---|---|---|---|
| Taft | 0.6459 | 0.6509 | 0.6819 | 0.7726 | 0.6919 | 3.0309 |
| Hector Mine | 0.6501 | 0.6114 | 0.7287 | 0.8096 | 0.7599 | 2.9732 |
| Loma Prieta | 0.6090 | 0.5713 | 0.6862 | 0.7316 | 0.6993 | 3.0155 |
| Average | 0.6350 | 0.6112 | 0.6989 | 0.7713 | 0.7170 | 3.0065 |

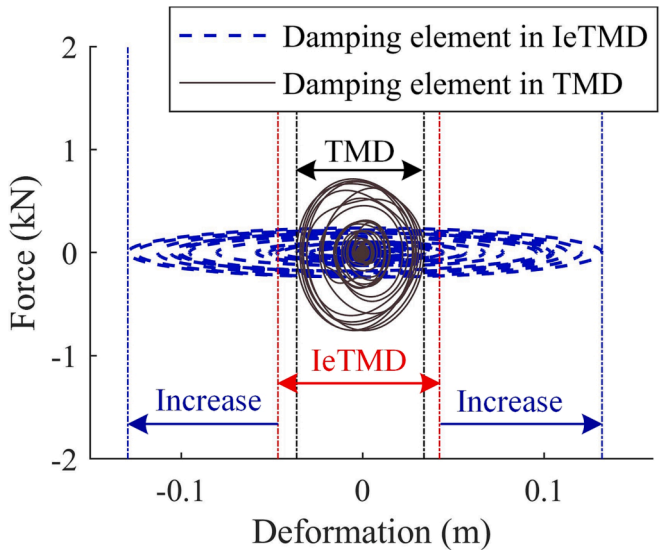


**Fig. 16.** Hysteretic curves of damping elements in the IeTMD and TMD.

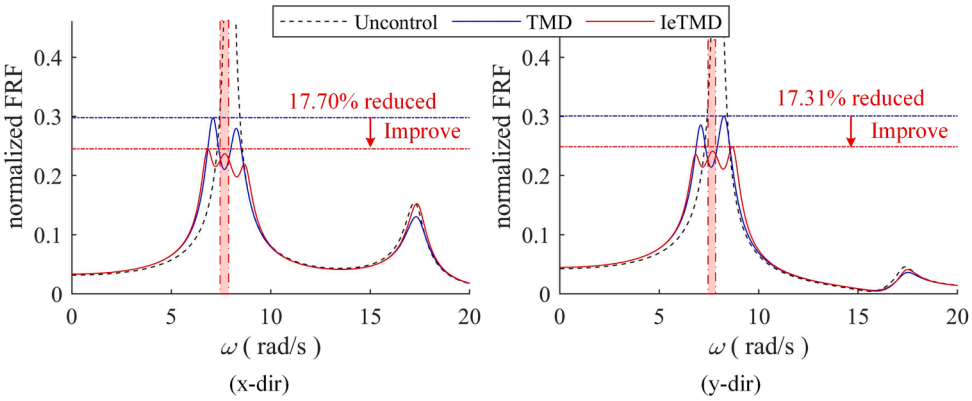


**Fig. 17.** Normalized FRFs of the controlled and uncontrolled domes (Node 4).

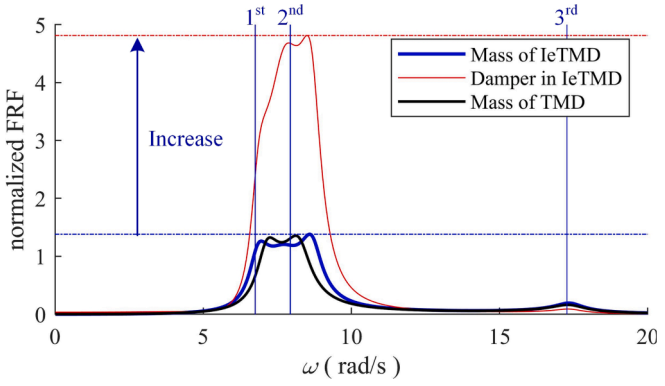


**Fig. 18.** Normalized FRFs for the suspension mass, damper of IeTMD and TMD.

## 5. Conclusions

In this study, we proposed the simplified design formulae of IeTMDs for the long-span domes by following the lightweight-based seismic vibration control criterion. The main findings are outlined as follows:

(1) The IeTMD is systematically verified to be highly effective in mitigating various seismic responses of long-span domes, including bi-directional displacements, accelerations, and base shear responses. Furthermore, the IeTMD provides similar control effectiveness as the TMD while reducing suspension mass by approximately 20 %. It demonstrates the IeTMD's potential as a promising solution for enhancing the seismic performance of long-span domes, particularly in situations where weight limitations are a concern.

(2) The suggested lightweight-control-oriented design methodology and empirical formulas for the IeTMD prove to be highly efficient and practical for attaining the desired control performance with minimal suspension mass.

(3) The IeTMD, designed by the provided formulae within the lightweight-control design framework, exhibits a wider control frequency band than traditional TMDs due to the double-tuned coupling effect of its inerter-based subsystem. Therefore, a well-designed IeTMD is suitable for controlling long-span dome structures' closely spaced participation modes.

(4) Although our discussion has focused on a particular IeTMD variant with a configuration similar to RIDTMD, it is essential to recognize that the core concept of IeTMDs, namely, the utilization of an inerter-based subsystem, to enhance damping as well as inertial effects and introduce additional degrees of freedom, remains consistent across different variations. Therefore, the lightweight-control-oriented design approach presented in this paper has the potential for application in other IeTMD variants for long-span domes.

(5) In this study, we focused on a linear IeTMD system. Nonetheless, practical devices may exhibit nonlinear effects stemming from friction and backlash, which necessitate further investigation. Moreover, during severe earthquakes, the assumption of linear behavior in long-span domes is no longer valid. Consequently, the

**Table 5**
Control performance of IeTMD and TMD.

| Ground motion | IeTMD $\gamma_p$ | TMD $\gamma_p$ | $\alpha_\gamma$(%) |
|---|---|---|---|
| Taft | 0.651 | 0.690 | 6.00 |
| Hector Mine | 0.611 | 0.675 | 10.47 |
| Loma Prieta | 0.571 | 0.634 | 11.03 |
| Average | 0.611 | 0.666 | 9.00 |

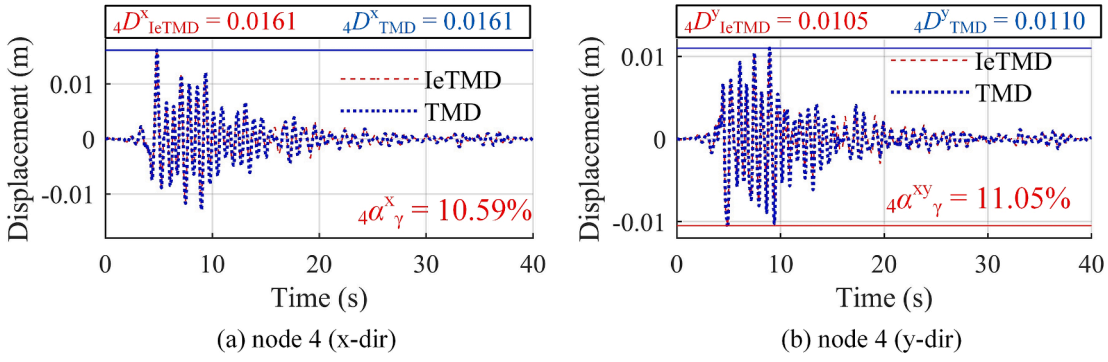


(a) node 4 (x-dir) (b) node 4 (y-dir)

**Fig. 19.** Comparison of the responses of the domes controlled by IeTMD and TMD.

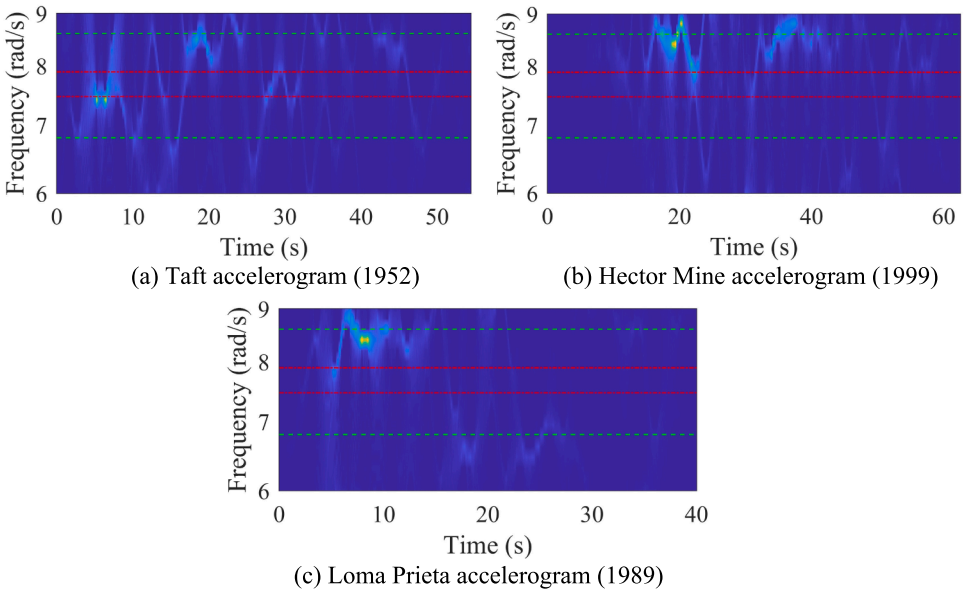


**Fig. 20.** The wavelet transform of displacement responses of the long-span dome controlled by IeTMD (Node 4).

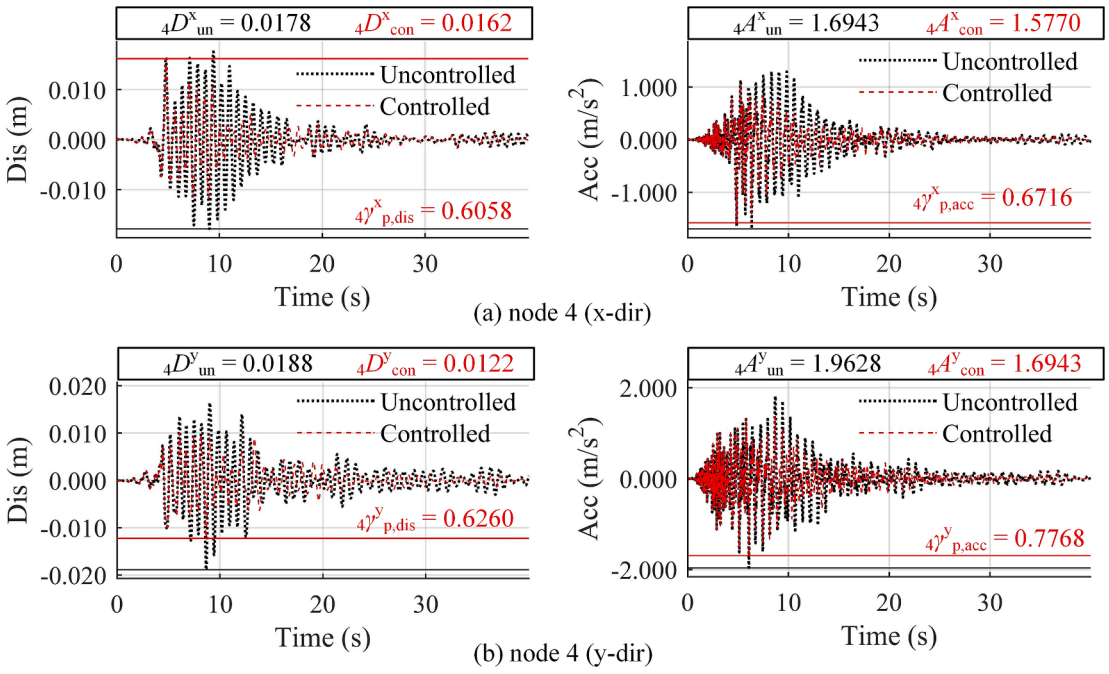


**Fig. 21.** Displacement and acceleration responses considering bi-directional seismic effect.

**Table 6**
Mitigation ratios considering horizontal and bi-directional seismic effects.

| Ground motion | $\gamma^x_{p,dis}$ | $\gamma^y_{p,dis}$ | $\gamma^x_{p,acc}$ | $\gamma^y_{p,acc}$ | $\gamma_{p,shear}$ | $\gamma_d$ |
|---|---|---|---|---|---|---|
| Horizontal | 0.6090 | 0.5713 | 0.6862 | 0.7316 | 0.6993 | 3.0155 |
| Bi-directional | 0.6102 | 0.6858 | 0.6872 | 0.7928 | 0.6993 | 2.9532 |

impact of material and geometric nonlinearity due to significant deformations on the performance of IeTMDs requires further quantification. These pertinent concerns will be addressed in future studies, employing both theoretical and experimental analyses.

## Declaration of Competing Interest

The authors declare that they have no known competing financial interests or personal relationships that could have appeared to influence the work reported in this paper.

## Funding

This study was supported by the National Key R&D Program of China (Grant No.2021YFE0112200) and the Natural Science Foundation of Shanghai (Grant No. 20ZR1461800).

## References


[1] Bradshaw R, Campbell D, Gargari M, Mirmiran A, Tripeny P. Special structures: Past, Present, and Future. Journal of Structural Engineering 2002;128:691–709. https://doi.org/10.1061/(ASCE)0733-9445(2002)128:6(691).

[2] Kawashima K, Kanoh T. Evaluation of indirect economic effects caused by the 1983 Nihonkai-chubu, Japan. Earthquake Earthq Spectra 1990;6:739–56. https://doi.org/10.1193/1.1585594.

[3] Kawaguchi K. A report on large roof structures damaged by the Great Hanshin-Awaji Earthquake. International Journal of Space Structures 1997;12:135–47. https://doi.org/10.1177/026635119701200303.

[4] Ishikawa K, Kato S, Elastic-plastic dynamic buckling analysis of reticular domes subjected to earthquake motion, Int J Space Struct, 1997; vol. 12 (3–4): 205–215. https://doi: 10.1177/026635119701200309.

[5] Kato S, Ueki T, Mukaiyama Y. Study of dynamic collapse of single layer reticular domes subjected to earthquake motion and the estimation of statically equivalent seismic forces. International Journal of Space Structures 1997;12:191–203. https://doi.org/10.1177/026635119701200308.

[6] Zhi XD, Nie GB, Fan F, Shen SZ. Vulnerability and risk assessment of single-layer reticulated domes subjected to earthquakes. Journal of Structural Engineering 2012;138:1505–14. https://doi.org/10.1061/(ASCE)ST.1943-541X.0000589.

[7] Kato S. Dr Mamoru Kawaguchi: His grand thought, prominent works, and contribution to the advancement of spatial structures. International Journal of Space Structures 2020;35:12–27. https://doi.org/10.1177/0956059920926361.

[8] Nakamura H. Preliminary report on the Great Hanshin Earthquake January 17, 1995. Japan Society of Civil Engineers; 1995.

[9] Feng Y, Liu Y, Xiao K. Experience the Wenchuan Earthquake—Structural engineers' point and view. Beijing: China Architecture and Building Press; 2009.

[10] Mimura N, Yasuhara K, Kawagoe S, Yokoki H, Kazama S. Damage from the Great East Japan Earthquake and Tsunami - A quick report. Mitig Adapt Strat Gl 2011;16:803–18. https://doi.org/10.1007/s11027-011-9297-7.

[11] Li H, Zhao L, Huang R, Hu Q. Hierarchical earthquake shelter planning in urban areas: A case for Shanghai in China. International Journal of Disaster Risk Reduction 2017;22:431–46. https://doi.org/10.1016/j.ijdrr.2017.01.007.

[12] Takeuchi T, Ogawa T, Yamagata C, Kumagai T. Response evaluation of cylindrical lattice shell roofs with supporting substructures. J Struct Constr Eng 2005;70:57–64. https://doi.org/10.3130/aijs.70.57_4.

[13] Takeuchi T, Ogawa T, Kumagai T. Seismic response evaluation of lattice shell roofs using amplification factors. J Int Assoc Shell Spat Struct 2007;48:197–210.

[14] Li QS, Chen JM. Nonlinear elastoplastic dynamic analysis of single-layer reticulated shells subjected to earthquake excitation. Computers and Structures 2003;81:177–88. https://doi.org/10.1016/S0045-7949(02)00445-5.

[15] Luo YF, Wang L, Guo XN. Threshold value method and its application in dynamic analysis of spatial latticed structures. Advances in Structural Engineering 2012;15:2215–26. https://doi.org/10.1260/1369-4332.15.12.2215.

[16] Nie G, Zhi X, Fan F, Dai J. Seismic performance evaluation of single-layer reticulated dome and its fragility analysis. Journal of Constructional Steel Research 2014;100:176–82. https://doi.org/10.1016/j.jcsr.2014.04.031.

[17] Liu W, Ye J. Collapse optimization for domes under earthquake using a genetic simulated annealing algorithm. Journal of Constructional Steel Research 2014;97:59–68. https://doi.org/10.1016/j.jcsr.2014.01.015.

[18] Ding Y, Chen Z-T, Zong L, Yan J-B. A theoretical strut model for severe seismic analysis of single-layer reticulated domes. Journal of Constructional Steel Research 2017;128:661–71. https://doi.org/10.1016/j.jcsr.2016.09.022.

[19] Nie G, Zhang C, Zhi X, Dai J. Collapse of the single layered cylinder shell with model experimental study. Arch Civ Mech Eng 2019;19:883–97. https://doi.org/10.1016/j.acme.2019.04.002.

[20] Yong-Chul K, Xue S, Zhuang P, Zhao W, Li C. Seismic isolation analysis of FPS bearings in spatial lattice shell structures. International Journal of Space Structures 2010;9:93–102. https://doi.org/10.1007/s11803-010-8108-6.

[21] Karoki KE, Shen L, Gong J. Capacity analysis, investigations and retrofitting of a long span steel grid hangar. Engineering Failure Analysis 2017;78:1–14. https://doi.org/10.1016/j.engfailanal.2017.02.012.

[22] Han Q, Jing M, Lu Y, Liu M. Mechanical behaviors of air spring-FPS three-dimensional isolation bearing and isolation performance analysis. Soil Dynamics and Earthquake Engineering 2021;149:106872. https://doi.org/10.1016/j.soildyn.2021.106872.

[23] Xu Z-D, Zhang T, Huang X-H. Dynamic analysis of three-directional vibration isolation and mitigation for long-span grid structure. Journal of Constructional Steel Research 2023;202:107758. https://doi.org/10.1016/j.jcsr.2022.107758.

[24] Tsuda S, Ohsaki M. Parameter optimization of mass damper consisting of compliant mechanism for bi-directional control of spatial structures. J Struct Constr Eng 1997;12:205–15. https://doi.org/10.3130/aijs.77.379.

[25] Yoshinaka S, Kawaguchi K. Vibration control of large span structures using spatially distributed MTMDs. J Struct Constr Eng 2008;73:1551–9. https://doi.org/10.3130/aijs.73.1551.

[26] Yamakawa M, Yoshinaka S, Araki Y, Uetani K, Kawaguchi K. Estimation of the global optimality for multiple tuned mass damper systems using order statistics. 11th World Congress on Computational Mechanics, WCCM 2014, 5th European Conference on Computational Mechanics, ECCM 2014 and 6th European Conference on Computational Fluid Dynamics, ECFD 2014, Barcelona, Spain: International Center for Numerical Methods in Engineering; 2014, p. 4362–72.

[27] Chen M, Papageorgiou C, Scheibe F, Wang F, Smith M. The missing mechanical circuit element. IEEE Circ Syst Mag 2009;9:10–26. https://doi.org/10.1109/MCAS.2008.931738.

[28] Lu L, Duan Y-F, Spencer BF, Lu X, Zhou Y. Inertial mass damper for mitigating cable vibration. Structural Control and Health Monitoring 2017;24:e1986.

[29] Zuo H, Bi K, Hao H, Ma R. Influences of ground motion parameters and structural damping on the optimum design of inerter-based tuned mass dampers. Engineering Structures 2021;227:111422. https://doi.org/10.1016/j.engstruct.2020.111422.

[30] Ma R, Bi K, Hao H. Inerter-based structural vibration control: A state-of-the-art review. Engineering Structures 2021;243:112655. https://doi.org/10.1016/j.engstruct.2021.112655.

[31] Shen W, Long Z, Cai L, Niyitangamahoro A, Zhu H, Li Y, et al. An inerter-based electromagnetic damper for civil structures: Modeling, testing, and seismic performance. Mech Syst Signal Pr 2022;173:109070. https://doi.org/10.1016/j.ymssp.2022.109070.

[32] Dai K, Jiang Z, Fang C, Li P, Zhang S. A tuned cable-inerter system for vibration reduction of towers. International Journal of Mechanical Sciences 2023;248:108199. https://doi.org/10.1016/j.ijmecsci.2023.108199.

[33] Zhao Z, Hu X, Zhang R, Chen Q. Analytical optimization of the tuned viscous mass damper under impulsive excitations. International Journal of Mechanical Sciences 2022;228:107472.

[34] Kang J, Ikago K. Seismic control of multidegree-of-freedom structures using a concentratedly arranged tuned viscous mass damper. Earthq Engng Struct Dyn 2023:eqe.3977. https://doi.org/10.1002/eqe.3977.

[35] Kawamata S. Accelerated liquid mass damper and principles of structural vibration control. Transactions of the International Conference on Structural Mechanics in Reactor Technology, Lausanne: 1987, p. 737–42.

[36] Arakaki T, Kuroda H, Arima F, Inoue Y, Baba K. Development of seismic devices applied to ball screw: Part 1 Basic performance test of RD-series. AIJ J Technol Des 1999;5:239–44. https://doi.org/10.3130/aijt.5.239_1.

[37] Arakaki T, Kuroda H, Arima F, Inoue Y, Baba K. Development of seismic devices applied to ball screw: Part 2 Performance test and evaluation of RD-series. AIJ J Technol Des 1999;5:265–70. https://doi.org/10.3130/aijt.5.265.

[38] Saito K, Inoue N. A study on optimum response control of passive control systems using viscous damper with inertial mass. J Technol Des 2007;13:457–62. https://doi.org/10.3130/aijt.13.457.

[39] Ikago K, Saito K, Inoue N. Seismic control of single-degree-of-freedom structure using tuned viscous mass damper. Earthq Eng Struct D 2012;41:453–74. https://doi.org/10.1002/eqe.1138.

[40] Sugimura Y, Goto W, Tanizawa H, Saito K, Ninomiya T, Nagasaku T. Response control effect of steel building structure using tuned viscous mass damper. Proceedings of the 15th World Conference on Earthquake Engineering, Lisbon, Portugal: 2012, p. ID 0138.

[41] Ogino M, Sumiyama T. Structural design of a high-rise building using tuned viscous mass dampers installed across three consecutive storeys. Civil-Comp Proceedings, Naples, Italy: 2014, p. 225. https://doi.org/10.4203/ccp.106.225.

[42] Lazar IF, Neild SA, Wagg DJ. Using an inerter-based device for structural vibration suppression. Earthq Eng Struct D 2014;43:1129–47. https://doi.org/10.1002/eqe.2390.

[43] Zhang R, Zhao Z, Pan C, Ikago K, Xue S. Damping enhancement principle of inerter system. Structural Control and Health Monitoring 2020;27:e2523.

[44] Djerouni S, Abdeddaim M, Elias S, Rupakhety R. Optimum double mass tuned damper inerter for control of structure subjected to ground motions. J Build Eng 2021;44:103259. https://doi.org/10.1016/j.jobe.2021.103259.

[45] Djerouni S, Elias S, Abdeddaim M, Domenico DD. Effectiveness of optimal shared multiple tuned mass damper inerters for pounding mitigation of adjacent buildings. Pract Period Struct Des 2023;28:04022063. https://doi.org/10.1061/(ASCE)SC.1943-5576.0000732.

[46] Giaralis A, Taflanidis AA. Optimal tuned mass-damper-inerter (TMDI) design for seismically excited MDOF structures with model uncertainties based on reliability criteria. Structural Control and Health Monitoring 2018;25:e2082.

[47] De Domenico D, Qiao H, Wang Q, Zhu Z, Marano G. Optimal design and seismic performance of Multi-Tuned Mass Damper Inerter (MTMDI) applied to adjacent high-rise buildings. Struct Des Tall Spec 2020;29:e1781.

[48] Garrido H, Curadelli O, Ambrosini D. Improvement of tuned mass damper by using rotational inertia through tuned viscous mass damper. Engineering Structures 2013;56:2149–53. https://doi.org/10.1016/j.engstruct.2013.08.044.

[49] Barredo E, Blanco A, Colín J, Penagos VM, Abúndez A, Vela LG, et al. Closed-form solutions for the optimal design of inerter-based dynamic vibration absorbers. International Journal of Mechanical Sciences 2018;144:41–53. https://doi.org/10.1016/j.ijmecsci.2018.05.025.

[50] Barredo E, Mendoza Larios JG, Mayén J, Flores-Hernández AA, Colín J, Arias MM. Optimal design for high-performance passive dynamic vibration absorbers under random vibration. Engineering Structures 2019;195:469–89. https://doi.org/10.1016/j.engstruct.2019.05.105.

[51] Barredo E, Mendoza Larios JG, Colín J, Mayén J, Flores-Hernández AA, Arias-Montiel M. A novel high-performance passive non-traditional inerter-based dynamic vibration absorber. Journal of Sound and Vibration 2020;485:115583. https://doi.org/10.1016/j.jsv.2020.115583.

[52] Zhang R, Zhao Z, Dai K. Seismic response mitigation of a wind turbine tower using a tuned parallel inerter mass system. Engineering Structures 2019;180:29–39. https://doi.org/10.1016/j.engstruct.2018.11.020.

[53] Zhang R, Cao Y, Dai K. Response control of wind turbines with ungrounded tuned mass inerter system (TMIS) under wind loads. Wind and Structures 2021;32:573–86. https://doi.org/10.12989/was.2021.32.6.573.

[54] Zhang Z, Larsen TG. Optimal calibration of the rotational inertia double tuned mass damper (RIDTMD) for rotating wind turbine blades. Journal of Sound and Vibration 2021;493:115827. https://doi.org/10.1016/j.jsv.2020.115827.

[55] Chopra AK. Dynamics of structures. 4th edition. Upper Saddle River, N.J: Pearson; 2011.
[56] Lutes LD, Sarkani S. Random vibrations: analysis of structural and mechanical systems. 1st edition. Butterworth-Heinemann; 2003.
[57] Pan C, Zhang R. Design of structure with inerter system based on stochastic response mitigation ratio. Structural Control and Health Monitoring 2018;25: e2169.
[58] The MathWorks Inc. Optimization Toolbox version: 9.4 (R2022b). Natick, Massachusetts: The MathWorks Inc.; 2022.
[59] Taniguchi T, Der Kiureghian A, Melkumyan M. Effect of tuned mass damper on displacement demand of base-isolated structures. Soil Dynamics and Earthquake Engineering 2008;30:3478–88. https://doi.org/10.1016/j.engstruct.2008.05.027.
[60] Taniguchi T, Der Kiureghian A, Melkumyan M, De Domenico D, Ricciardi G. Earthquake-resilient design of base isolated buildings with TMD at basement: Application to a case study. Soil Dynamics and Earthquake Engineering 2018;113: 503–21. https://doi.org/10.1016/j.soildyn.2018.06.022.